JCI The Journal of Clinical Investigation

Calpain-6 confers atherogenicity to macrophages by dysregulating pre-mRNA splicing

Takuro Miyazaki, … , Hiroki Kurihara, Akira Miyazaki

J Clin Invest. 2016;126(9):3417-3432. https://doi.org/10.1172/JCI85880.

Research Article **Vascular biology**

Macrophages contribute to the development of atherosclerosis through pinocytotic deposition of native LDL–derived cholesterol in macrophages in the vascular wall. Inhibiting macrophage-mediated lipid deposition may have protective effects in atheroprone vasculature, and identifying mechanisms that potentiate this process may inform potential therapeutic interventions for atherosclerosis. Here, we report that dysregulation of exon junction complex–driven (EJC-driven) mRNA splicing confers hyperpinocytosis to macrophages during atherogenesis. Mechanistically, we determined that inflammatory cytokines induce an unconventional nonproteolytic calpain, calpain-6 (CAPN6), which associates with the essential EJC-loading factor CWC22 in the cytoplasm. This association disturbs the nuclear localization of CWC22, thereby suppressing the splicing of target genes, including those related to Rac1 signaling. CAPN6 deficiency in LDL receptor–deficient mice restored CWC22/EJC/Rac1 signaling, reduced pinocytotic deposition of native LDL in macrophages, and attenuated macrophage recruitment into the lesions, generating an atheroprotective phenotype in the aorta. In macrophages, the induction of CAPN6 in the atheroma interior limited macrophage movements, resulting in a decline in cell clearance from the lesions. Consistent with this finding, we observed that myeloid CAPN6 contributed to atherogenesis in a murine model of bone marrow transplantation. Furthermore, macrophages from advanced human atheromas exhibited increased CAPN6 induction and impaired CWC22 nuclear localization. Together, these results indicate that CAPN6 promotes atherogenicity in inflamed macrophages by disturbing CWC22/EJC systems.

Calpain-6 confers atherogenicity to macrophages by dysregulating pre-mRNA splicing

Takuro Miyazaki,[1] Kazuo Tonami,[2] Shoji Hata,[3] Toshihiro Aiuchi,[4] Koji Ohnishi,[5] Xiao-Feng Lei,[1] Joo-ri Kim-Kaneyama,[1] Motohiro Takeya,[5] Hiroyuki Itabe,[4] Hiroyuki Sorimachi,[3] Hiroki Kurihara,[2] and Akira Miyazaki[1]

[1]Department of Biochemistry, Showa University School of Medicine, Tokyo, Japan. [2]Department of Physiological Chemistry and Metabolism, Graduate School of Medicine, The University of Tokyo, Tokyo, Japan. [3]Calpain Project, Department of Advanced Science for Biomolecules, Tokyo Metropolitan Institute of Medical Science, Tokyo, Japan. [4]Division of Biological Chemistry, Department of Molecular Biology, Showa University School of Pharmacy, Tokyo, Japan. [5]Department of Cell Pathology, Graduate School of Medical Sciences, Kumamoto University, Kumamoto, Japan.

Macrophages contribute to the development of atherosclerosis through pinocytotic deposition of native LDL–derived cholesterol in macrophages in the vascular wall. Inhibiting macrophage-mediated lipid deposition may have protective effects in atheroprone vasculature, and identifying mechanisms that potentiate this process may inform potential therapeutic interventions for atherosclerosis. Here, we report that dysregulation of exon junction complex–driven (EJC-driven) mRNA splicing confers hyperpinocytosis to macrophages during atherogenesis. Mechanistically, we determined that inflammatory cytokines induce an unconventional nonproteolytic calpain, calpain-6 (CAPN6), which associates with the essential EJC-loading factor CWC22 in the cytoplasm. This association disturbs the nuclear localization of CWC22, thereby suppressing the splicing of target genes, including those related to Rac1 signaling. CAPN6 deficiency in LDL receptor–deficient mice restored CWC22/EJC/Rac1 signaling, reduced pinocytotic deposition of native LDL in macrophages, and attenuated macrophage recruitment into the lesions, generating an atheroprotective phenotype in the aorta. In macrophages, the induction of CAPN6 in the atheroma interior limited macrophage movements, resulting in a decline in cell clearance from the lesions. Consistent with this finding, we observed that myeloid CAPN6 contributed to atherogenesis in a murine model of bone marrow transplantation. Furthermore, macrophages from advanced human atheromas exhibited increased CAPN6 induction and impaired CWC22 nuclear localization. Together, these results indicate that CAPN6 promotes atherogenicity in inflamed macrophages by disturbing CWC22/EJC systems.

Introduction

Atherosclerosis is a vascular disease characterized by intimal and subintimal cholesterol deposition in which cholesterol forms an initial fatty streak that is followed by an extended atheroma (1). Rupture of atherosclerotic plaques leads to lethal cardiovascular events, such as myocardial infarction and stroke, 2 primary causes of morbidity and mortality worldwide. Pharmacotherapy using statins is beneficial for the primary prevention of cardiovascular diseases, achieving a reduction in event rates of approximately 20%–40% in randomized, placebo-controlled clinical trials (2); however, statins are insufficient for lowering the number of recurrent events. For instance, lethal recurrent ischemic events following acute coronary syndrome occur in more than 20% of patients by 30 months despite optimal cholesterol-lowering therapy (3). Thus, a precise understanding of the pathogenesis of atherosclerotic diseases in vascular walls, including cholesterol deposition, is indispensable for next-generation antiatherosclerosis therapies.

Cholesterol deposition in vascular walls is mainly due to foam cell formation within monocyte-derived macrophages (4). Although many earlier investigations are based on the concept that foam cell formation in macrophages is driven by the uptake of oxidized LDLs by scavenger receptors, some findings challenge this hypothesis. For instance, LDL isolated from human atherosclerotic vessels is insufficiently oxidized to be recognized by scavenger receptors (5). Furthermore, a deficiency of scavenger receptors does not abrogate foam cell formation in macrophages in atherogenic mice (6), implying that alternative mechanisms govern LDL uptake in macrophages. Recent advances have shown that scavenger receptor–independent uptake of native LDL in macrophages can drive foam cell formation. This phenomenon is known as fluid-phase pinocytosis (7). The pinocytotic uptake of native LDL is also independent of the degree of LDL oxidation and does not saturate, which is distinct from the properties of receptor-mediated uptake of modified LDL. Buono et al. reported that pinocytotic activity is potentiated in macrophages in murine atherosclerotic lesions (8). Although pinocytosis is mediated through Rho GTPase cytoskeletal dynamics (9, 10), little is known about its regulatory mechanisms.

In macrophage biology, growing evidence suggests that the posttranslational processing of functional proteins, in addition to their transcriptional regulation, defines their physiological and pathophysiological behavior. Calpain, an intracellular Ca^{2+}-sensitive protease, plays a pivotal role in this process, thereby controlling endocytic signals in macrophages (11) and intracellular trafficking in platelets (12) as well as cytoskeletal dynamics (13). In terms of cholesterol regulation, calpain-1 (μ-calpain) reportedly proteolyzes

Conflict of interest: The authors have declared that no conflict of interest exists.
Submitted: December 4, 2015; **Accepted:** July 7, 2016.
Reference information: *J Clin Invest*. 2016;126(9):3417–3432. doi:10.1172/JCI85880.

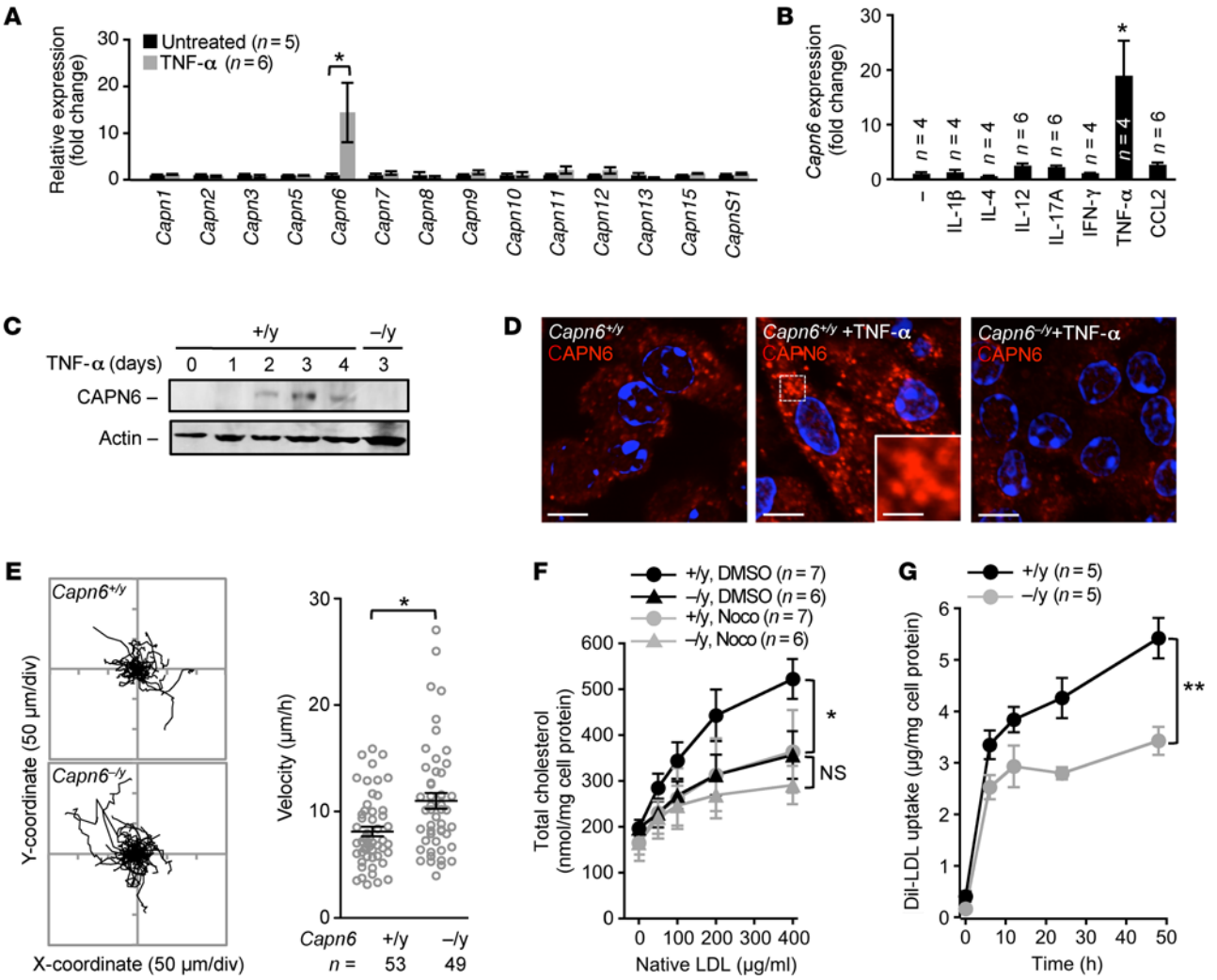

Figure 1. Loss of CAPN6 reduces the pinocytotic uptake of native LDL in macrophages. BMMs at day 4 of differentiation were used in these experiments. (**A**) Expression of calpain family members in BMMs in response to TNF-α stimulus. (**B**) Expression of *Capn6* mRNA in BMMs in response to variety of inflammatory stimuli. BM cells were stimulated with a variety of cytokines (IL-1β, IL-4, IL-12, IL-17A, IFN-γ, TNF-α, 10 ng/ml; or CCL2, 50 ng/ml) together with M-CSF at 50 ng/ml for 4 days. (**C**) CAPN6 protein expression in TNF-α/M-CSF–primed BMMs. One representative result of 3 independent experiments is shown. (**D**) Subcellular distribution of CAPN6 in TNF-α/M-CSF–primed *Capn6*$^{+/y}$*Ldlr*$^{-/-}$ BMMs. *Capn6*$^{-/y}$*Ldlr*$^{-/-}$ BMMs served as a negative control. Scale bars: 10 μm (**D**); 3 μm (insets).(**E**) Cellular movements in BMMs. TNF-α/M-CSF–primed BMMs were tracked for 10 hours in the presence of CCL2 at 50 ng/ml. (**F**) Uptake of native LDL in TNF-α/M-CSF–primed *Capn6*$^{+/y}$*Ldlr*$^{-/-}$ or *Capn6*$^{-/y}$*Ldlr*$^{-/-}$ BMMs. Cells were treated with native LDL for 24 hours at the concentrations indicated, either in the presence of DMSO or nocodazole (Noco) at 1 μmol/l. (**G**) Temporal changes in the uptake of DiI-labeled LDL in TNF-α/M-CSF–primed BMMs. $^{**}P < 0.01$; $^{*}P < 0.05$, 1-way ANOVA followed by Bonferroni's test (**A** and **B**), Mann–Whitney *U* test (**E**), 2-way ANOVA (**F** and **G**). Error bars represent the mean ± SEM.

the proteins ATP-binding cassette transporter subfamily A member 1 (ABCA1) and ATP-binding cassette transporter subfamily G member 1 (ABCG1), thereby preventing cholesterol efflux in cultured macrophages (14, 15). Earlier investigations by others and us have suggested that administering subtype-nonselective inhibitors of calpains suppresses atherogenesis in mice without altering plasma dyslipidemia (16, 17). These atheroprotective actions may be due to the suppression of hyperpermeability induced by calpain-2 (m-calpain) in vascular endothelial cells and calpain-1–induced hyperinflammation in macrophages, whereas the proatherogenic roles of calpain in lipid handling in macrophages remain enigmatic. Moreover, considering that there are 15 homologues of the catalytic subunit of human calpain (13), the predominance of calpain family members in macrophage regulation remains unclear. Using gene-targeting approaches, we herein investigated the impact of calpain family members on LDL uptake in proatherogenic macrophages. This study identifies calpain-6 (CAPN6), a unique nonclassical calpain without proteolytic activity, as an accelerator of the pinocytotic deposition of native LDL in macrophages and proposes a mechanism involving LDL metabolism in macrophages that is inducible by the disturbance of posttranscriptional mRNA splicing.

Results

CAPN6 modulates Rac1-dependent cellular dynamics and pinocytotic activity. To examine the involvement of calpains in macrophage regulation, we investigated the expression of calpain family members in murine BM-derived macrophages (BMMs) (Figure 1A). *Capn6* mRNA was selectively induced by supplementing the

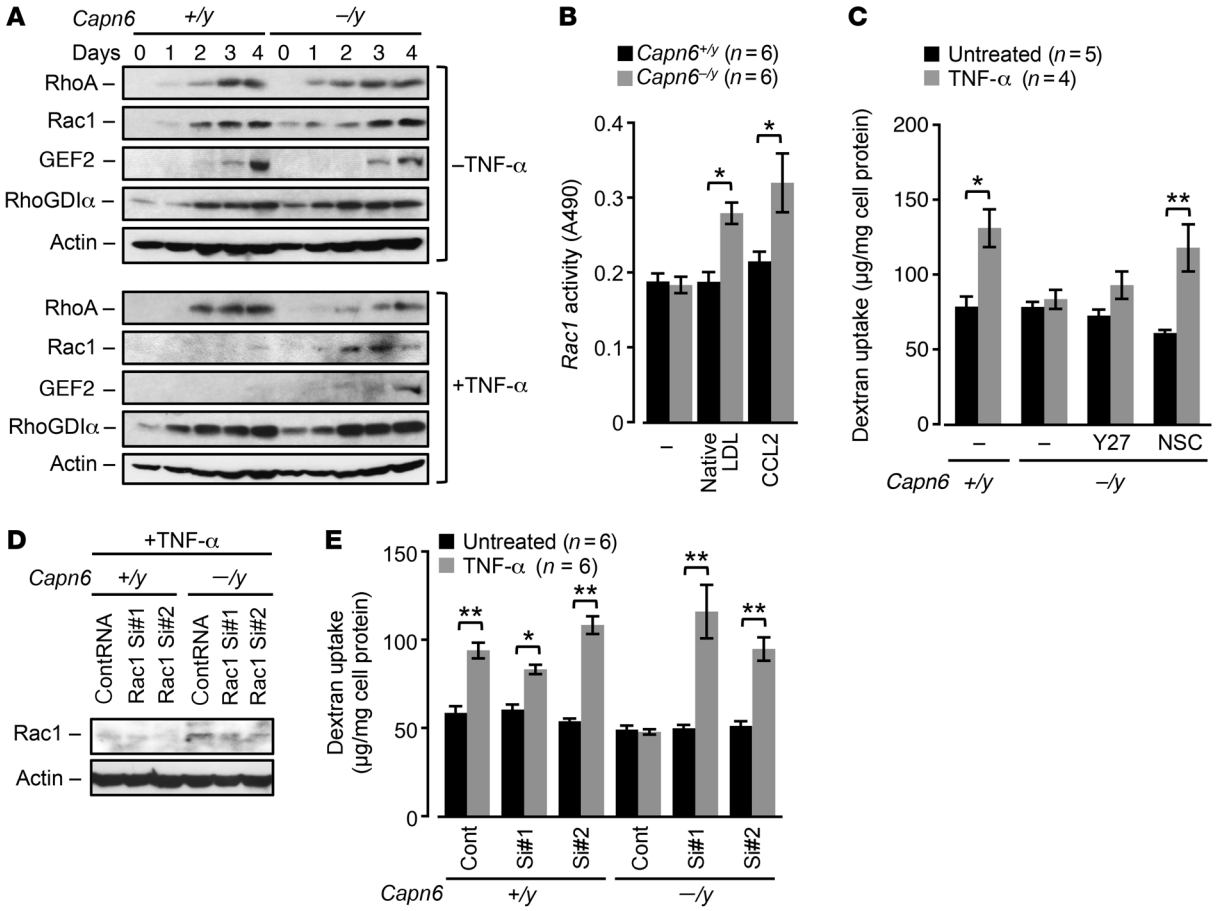

Figure 2. Recovery of *Rac1* by CAPN6 deficiency antagonizes pinocytotic activity in macrophages. BMMs differentiated with M-CSF/TNF-α for 4 days were utilized in these experiments. (**A**) Expression of Rho GTPases and their regulatory molecules in *Capn6*$^{+/y}$*Ldlr*$^{-/-}$ or *Capn6*$^{-/y}$*Ldlr*$^{-/-}$ BMMs. Cells were stimulated with 10 ng/ml TNF-α for the indicated time periods. One representative result of 3 independent experiments is shown. (**B**) *Rac1* activity in *Capn6*$^{+/y}$*Ldlr*$^{-/-}$ or *Capn6*$^{-/y}$*Ldlr*$^{-/-}$ BMMs. TNF-α–primed BMMs were stimulated with CCL2 at 50 ng/ml or native LDL at 400 μg/ml for 20 minutes. (**C**) Pinocytotic activity in *Capn6*-deficient BMMs. Cells were pretreated with y-27632 at 10 μmol/l or NSC23766 at 50 μmol/l for 1 hour. (**D**) Silencing of endogenous Rac1 protein by siRNA. One representative result of 3 independent experiments is shown. (**E**) Effects of *Rac1* silencing on pinocytotic activity in *Capn6*-deficient BMMs. $^{**}P < 0.01$; $^{*}P < 0.05$, 1-way ANOVA followed by Bonferroni's test (**B**, **C** and **E**); error bars represent mean ± SEM.

culture medium with TNF-α and macrophage CSF (M-CSF). Next, BMMs were stimulated with TNF-α, IFN-γ, IL-1β, IL-4, IL-12, IL-17A, or chemokine (C-C motif) ligand 2 (CCL2, also known as monocyte chemoattractant protein-1), together with M-CSF (Figure 1B). *Capn6* mRNA was increased 2- to 3-fold by IL-12, IL-17A, or CCL2, whereas it was elevated 15- to 20-fold by TNF-α. *Capn6* mRNA expression in M-CSF/TNF-α–primed BMMs reflected the changes in its protein, which was abolished by a deficiency of *Capn6* (Figure 1C). Then TNF-α–stimulated expression of CAPN6 was induced in J774 macrophages and THP-1 cells (Supplemental Figure 1, A and B; supplemental material available online with this article; doi:10.1172/JCI85880DS1). Immunocytochemical analysis showed that CAPN6 in M-CSF/TNF-α–primed BMMs is located in clusters in the cytoplasm (Figure 1D). CAPN6 did not exist in major intracellular vesicles involving pinosomes, endosomes, or mitochondria, whereas a small portion of CAPN6-positive vesicles was overlapped with lysosomes (Supplemental Figure 1C).

DNA array analysis showed that mRNA expression levels in M-CSF/TNF-α–primed BMMs were not comprehensively altered by *Capn6* deficiency (Supplemental Figure 1D); indeed, the expression ratio (*Capn6*$^{+/y}$*Ldlr*$^{-/-}$ versus *Capn6*$^{-/y}$*Ldlr*$^{-/-}$, where *Ldlr* indicates LDL receptor) of 93.3% of genes (55,359 of 59,305 genes) was within 2-fold. A PCR-based analysis confirmed that the expression levels of molecules related to the uptake of oxidized LDL (*Cd36*, *Msr1*, *Nr1h3*, *Abca1*, *Abcg1,* and *Acat1*) and markers for M1 (*Nos2*, *Tnf*, *Il1b,* and *Il6*) and M2 (*Arg1*) macrophages were comparable between *Capn6*$^{+/y}$*Ldlr*$^{-/-}$ and *Capn6*$^{-/y}$*Ldlr*$^{-/-}$ BMMs, even in the presence of M-CSF/TNF-α stimulus (Supplemental Figure 1E). In turn, *Capn6* deficiency accelerated cellular movements in M-CSF/TNF-α–primed BMMs in the presence of CCL2 (Figure 1E).

Next, we analyzed cholesterol handling in BMMs. The receptor-mediated uptake of oxidized LDL and engulfment of aggregated LDL in M-CSF/TNF-α–primed *Ldlr*$^{-/-}$ BMMs were not influenced by *Capn6* deficiency (Supplemental Figure 1, F and G, respectively); conversely, the pinocytotic uptake of native LDL in the cells was significantly downregulated by *Capn6* deficiency (Figure 1F). We confirmed that the uptake of native LDL in *Capn6*$^{+/y}$ *Ldlr*$^{-/-}$ BMMs was prevented by nocodazole-induced microtubule disorganization, as noted in previous studies (18). Similar nocodazole-induced prevention was undetectable in *Capn6*$^{-/y}$*Ldlr*$^{-/-}$

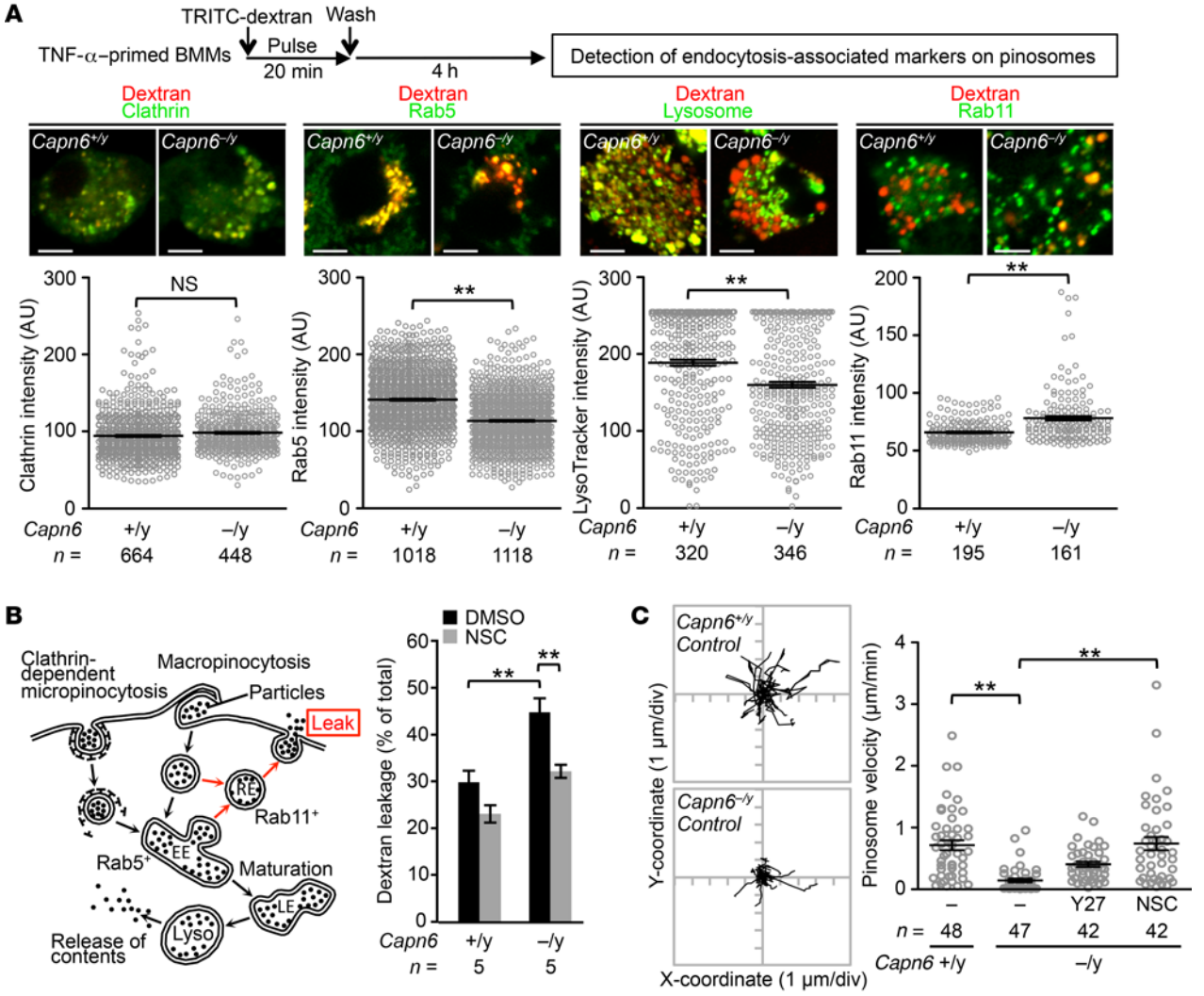

Figure 3. Loss of CAPN6 decelerates pinosome velocity and maturation and facilitates the leakage of pinocytotic particles in macrophages. (**A**) Pinosome maturity in *Capn6*-deficient BMMs. BMMs were fixed following pulsed application of TRITC-labeled dextran at 5 mg/ml for 30 minutes, and fluorescence intensity in individual pinosomes was measured. Scale bars: 5 μm. (**B**) Leakage of pinocytotic particles in BMMs. Spontaneous leakage of TRITC-labeled dextran for 24 hours was measured in the presence or absence of NSC23766 at 50 μmol/l. EE, early endosome; LE, late endosome; RE, recycling endosome; Lyso, lysosome. (**C**) Pinosome velocity in *Capn6*-deficient BMMs. Cells were pretreated with y-27632 at 10 μmol/l or NSC23766 at 50 μmol/l for 1 hour. $^{**}P < 0.01$, Mann–Whitney *U* test (**A**) and 1-way ANOVA followed by Bonferroni's test (**B** and **C**); error bars represent mean ± SEM.

BMMs. Consistently, uptake of Dil-labeled LDL in *Capn6*$^{-/y}$*Ldlr*$^{-/-}$ BMMs was lower than that in *Capn6*$^{+/y}$*Ldlr*$^{-/-}$ BMMs. It is likely that the uptake in *Capn6*$^{-/y}$*Ldlr*$^{-/-}$ BMMs was saturated within 12 hours following administration (Figure 1G). *Capn6* deficiency increased cholesterol efflux in the presence or absence of apoA-I (Supplemental Figure 1H), indicating that CAPN6 potentially weakens spontaneous cholesterol efflux, but not apoA-I–induced efflux.

We sought to determine the mechanisms underlying the changes in pinocytotic activity in *Capn6*$^{-/y}$*Ldlr*$^{-/-}$ BMMs. RhoA/Rac1 GTPases and their modulators, Rho/Rac guanine nucleotide exchange factor 2 (GEF2) and Rho GDP dissociation inhibitor α (RhoGDIα), were induced during differentiation in both *Capn6*$^{+/y}$*Ldlr*$^{-/-}$ and *Capn6*$^{-/y}$*Ldlr*$^{-/-}$ BMMs in the absence of TNF-α stimulus (Figure 2A). The induction of Rac1 and GEF2 in *Capn6*$^{+/y}$*Ldlr*$^{-/-}$ BMMs, but not of RhoA and RhoGDIα, was abolished by TNF-α stimulus, whereas the induction of Rac1 and GEF2 was rescued by *Capn6* deficiency. *Capn6*$^{-/y}$*Ldlr*$^{-/-}$ BMMs showed higher Rac1 activity in the presence of native LDL or CCL2 compared with *Capn6*$^{+/y}$*Ldlr*$^{-/-}$ BMMs, whereas the baseline activity of Rac1 was unaltered by *Capn6* deficiency (Figure 2B). Rac1 protein expression was independent of its mRNA expression (Supplemental Figure 2A).

We measured the uptake of fluorescent dextran in isolated BMMs as an index of macropinocytosis (Figure 2C). Macropinocytosis in *Capn6*$^{+/y}$*Ldlr*$^{-/-}$ BMMs was potentiated by TNF-α stimulus and attenuated by *Capn6* deficiency. This reduced pinocytotic activity in *Capn6*$^{-/y}$*Ldlr*$^{-/-}$ BMMs was rescued by NSC23766-induced inhibition of Rac1, but not by Y27632-induced inhibition of RhoA/Rho kinase signaling. Similarly, siRNA-based silencing of Rac1 recovered declined macropinocytosis in *Capn6*$^{-/y}$*Ldlr*$^{-/-}$ BMMs (Figure 2, D and E), while overexpression of wild-type Rac1 failed to decrease pinocytotic activity in *Capn6*$^{+/y}$*Ldlr*$^{-/-}$ BMMs (Supplemental Figure 2B). Furthermore, uptake of Lucifer

Table 1. Candidate CAPN6-associated proteins detected by IP–LC–MS/MS analysis

	Gene name	Gene ID	Cover (%)
Calpain-6	*Capn6*	12338	30.1
ADP/ATP translocase 1	*Slc25a4*	11739	23.5
Runt-related transcription factor 3	*Runx3*	12399	20.5
Jumonji, AT rich interactive domain 2	*Jarid2*	16468	18.2
CWC22 spliceosome-associated protein homolog	*Cwc22*	80744	16.0
Lysine (K)–specific demethylase 3A	*Kdm3a*	104263	4.8
DEAD (Asp-Glu-Ala-Asp) box polypeptide 5	*Ddx5*	13207	3.9
Ring finger protein 38	*Rnf38*	73469	2.9

yellow in BMMs was partially inhibited by *Capn6* deficiency, suggesting that *Capn6* contributes to micropinocytosis as well as macropinocytosis (Supplemental Figure 2C). Forced *Capn6* expression accelerated macropinocytosis in M-CSF/TNF-α–stimulated J774 macrophages, which was prevented by the broad-range small GTPase inhibitor *Clostridium difficile* toxin B (Supplemental Figure 2D). Consistently, forced expression of *Capn6* downregulated Rac1 expression in J774 cells, thereby decelerating CCL2-driven cellular movement (Supplemental Figure 2, E and F). *Capn6* deficiency potentiated other Rac1-associated events in BMMs, including generation of oxidative stress and efferocytic engulfment of apoptotic cells (Supplemental Figure 2, G and H, respectively), while the cellular mitosis remained unchanged (Supplemental Figure 2I).

At the initial stage of pinocytosis, plasma membrane is internalized as clathrin-coated vesicles (for micropinocytosis) or noncoated vesicles (for macropinocytosis), which subsequently fuse with early/late endosomes. The endosomes finally fuse with lysosomes to digest interior particles, thereby releasing and accumulating the particles into cytoplasm. Importantly, a portion of intracellular vesicles refuses with the plasma membrane, allowing the vesicles to be recycled. During this process, interior particles are released to the extracellular spaces. To evaluate the fate of pinosome, we visualized endosome-related markers on dextran-labeled pinosomes (Figure 3A). We showed that intensity of the early endosome marker RAB5 and lysosomal labeling with LysoTracker (Thermo Fisher Scientific) on pinosomes was reduced by *Capn6* deficiency; conversely, that of clathrin, a marker for clathrin-coated vesicles, was unchanged by *Capn6* deficiency. In contrast, recycling endosome marker RAB11 on pinosomes was increased by *Capn6* deficiency. Consistently, deficiency of *Capn6* facilitated the spontaneous leakage of fluorescent dextran from BMMs in a Rac1-dependent manner (Figure 3B). Real-time tracking of pinosomes showed that their velocity was reduced by *Capn6* deficiency (Figure 3C). Pinosome velocity in $Capn6^{-/y}Ldlr^{-/-}$ BMMs was recovered by NSC23766-induced inhibition of Rac1, but not by Y27632-induced inhibition of RhoA/Rho kinase signaling. Conversely, *Capn6* deficiency did not influence pinosome density (Supplemental Figure 3).

CAPN6 associates with CWC22, thereby interfering with the posttranscriptional regulation of Rac1 signaling. Next, we focused on how CAPN6 modulates Rac1 expression during macrophage differentiation. IP–liquid chromatography–mass spectrometry/mass spectrometry (IP–LC–MS/MS) analysis identified several CAPN6-associated molecules, including CWC22 spliceosome-associated protein homolog, an essential loading factor of exon junction complex (EJC) (Table 1). Physical linkage between CWC22 and CAPN6 was validated by IP-immunoblotting analysis (Figure 4A). Organelle fractionation showed that *Capn6* deficiency enhanced nuclear localization of CWC22 in response to a second administration of TNF-α to BMMs at day 3 (Figure 4B). Immunocytochemical analysis showed that nuclear localization of CWC22 was induced by IL-1β and IFN-γ in addition to TNF-α, whereas IL-4 elicited relatively weak nuclear localization (Figure 4C). CWC22 was uniformly expressed in the cytoplasm of M-CSF–primed BMMs, whereas it was clustered and colocalized with CAPN6-positive vesicles in the cytoplasm of M-CSF/TNF-α–primed BMMs (Figure 4D). Such TNF-α–induced clustering of CWC22 was canceled by *Capn6* deficiency (Figure 4E). A second administration of TNF-α to BMMs caused nuclear localization of CWC22, which was potentiated by *Capn6* deficiency (Figure 4E). In humans with atherosclerosis, significant nuclear localization of CWC22 in CD68-positive macrophages was detectable in mild-to-moderate atherosclerotic lesions; conversely, the localization was marginal in severe atherosclerotic lesions (Figure 5; clinicopathologic information is available in Supplemental Table 1). Thus, it is likely that the degree of CWC22 nuclear localization negatively correlates with the severity of atherosclerosis.

Because CWC22 is reportedly associated with EJC-mediated mRNA splicing (19), we assessed splicing efficiency in *Capn6*-deficient BMMs by a PCR-based analysis (Supplemental Figure 4 for detail). *Capn6* deficiency in M-CSF/TNF-α–primed BMMs elevated the ratio of spliced *Rac1, Arhgef2* (GEF2), and *Tpi1* mRNA to their pre-mRNAs, indicating improved mRNA splicing efficiency (Figure 6A); conversely, the splicing efficiency of *RhoA* and *Arhgdia* (RhoGDIa) mRNA remained unaffected. The elevation of *Rac1* splicing by *Capn6* deficiency was prevented by the siRNA-based silencing of *Cwc22* (Figure 6B). Accordingly, the induction of Rac1 protein in $Capn6^{-/y}Ldlr^{-/-}$ BMMs was reduced by the silencing of *Cwc22* (Figure 6C). Furthermore, *Cwc22* silencing reversed the phenotypic changes evident in *Capn6*-deficient BMMs, including the downregulation of pinocytotic activity (Figure 6D) and upregulation of cellular movements (Figure 6E).

Deficiency of macrophage CAPN6 suppresses proatherogenic pinocytosis. We compared the aortic expression of catalytic subunits of the calpain family in chow-fed and high-fat diet–fed (HFD-fed) $Ldlr^{-/-}$ mice. We found that the unconventional calpain genes *Capn6* and *Capn9* were induced in the aortas of HFD-fed mice in addition to the conventional *Capn2* (Figure 7A). Previously, we demonstrated that calpain-2 induction causes vascular endothelial cell hyperpermeability and subsequent atherosclerosis progression (16); thus, we attempted to focus on the roles of CAPN6 and CAPN9. *Capn6* deficiency in $Ldlr^{-/-}$ mice significantly inhibited the development of atherosclerotic lesions in the aorta independently of the sex of the mice (Figure 7B and Supplemental Figure 5A), whereas *Capn9* deficiency did not yield these atheroprotective effects (Supplemental Figure 5, B and C). *Capn6* deficiency did not alter blood glucose homeostasis (Supplemental Figure 5D), population of peripheral blood cells (Supplemental Figure

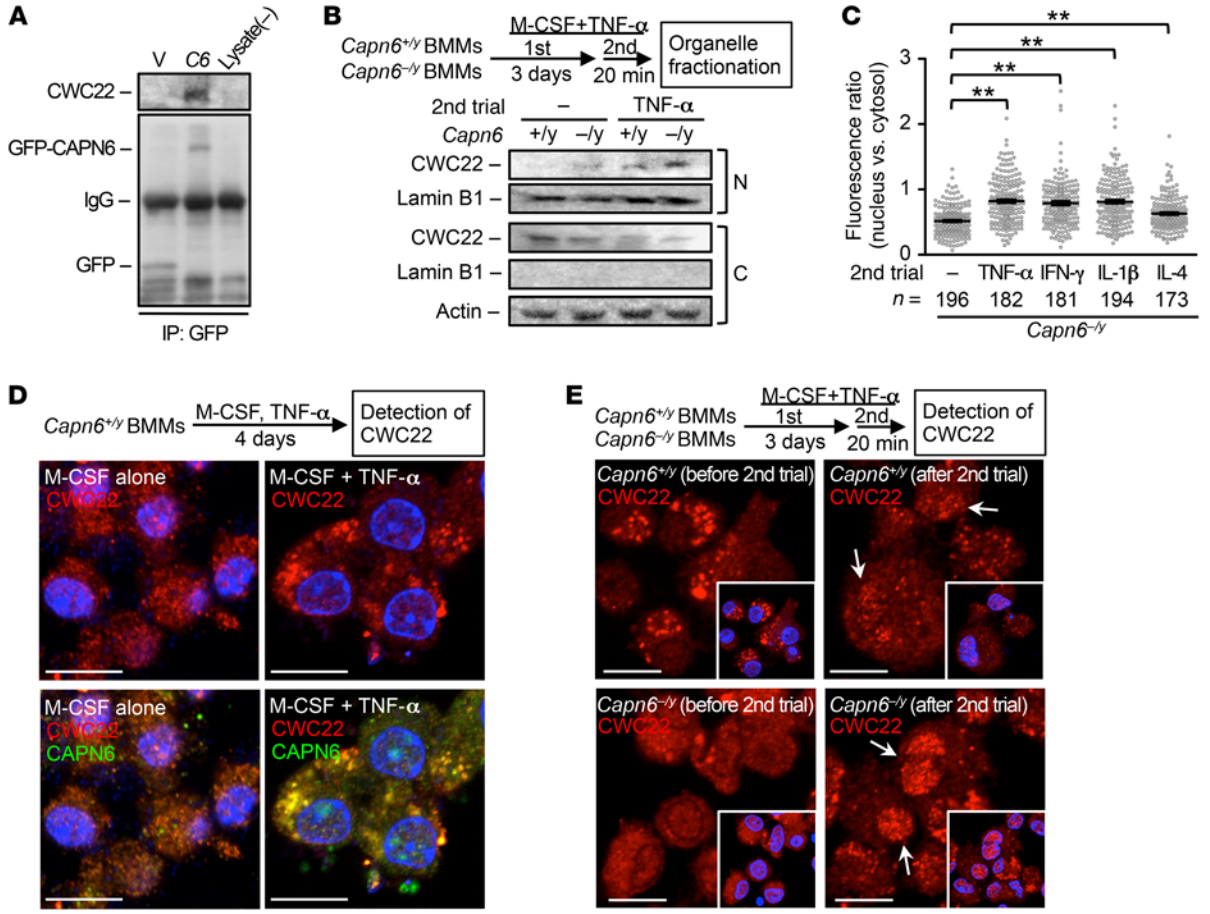

Figure 4. Nuclear localization of CWC22 in inflamed murine BMM is limited by the physical association between CAPN6 and CWC22. (**A**) CAPN6 associates with CWC22. Protein immunoprecipitates were detected by immunoblotting against CWC22 or GFP. One representative result of 3 independent experiments is shown. (**B**) *Capn6* deficiency potentiates nuclear localization of CWC22 in BMMs. After 20 minutes of a second administration of TNF-α/M-CSF, nuclear and cytoplasmic fractions were separated, and CWC22 was detected by immunoblotting. One representative result of 3 independent experiments is shown. N, nucleus; C, cytosol. (**C**) Nuclear localization of CWC22 in BMMs was induced by a variety of inflammatory cytokines. TNF-α–primed *Capn6*$^{-/y}$ *Ldlr*$^{-/-}$ BMMs were stimulated with a variety of cytokines for 20 minutes, and nuclear localization in individual cells was quantified. (**D**) Subcellular distribution of CWC22 in BMMs. BM cells were stimulated with M-CSF at 50 ng/ml in the presence or absence of TNF-α for 4 days; then CWC22 and CAPN6 were detected by immunocytochemistry. (**E**) *Capn6* deficiency potentiates nuclear localization of CWC22 in BMMs. BM cells were cultured in the presence of TNF-α at 10 ng/ml and M-CSF at 50 ng/ml for 3 days; then the culture medium was replaced with freshly prepared TNF-α/M-CSF–supplemented medium. Following 30-minute incubation, cells were fixed and CWC22 was detected by immunocytochemistry. Arrows represent nuclear localization of CWC22. $^{**}P < 0.01$, 1-way ANOVA followed by Bonferroni's test (**C**); error bars represent mean ± SEM. Scale bars: 10 μm (**D**); 10 μm (**E**).

5E), and oxidative stress in the lesions (Supplemental Figure 5F) and did not ameliorate plasma dyslipidemia (Figure 7C and Supplemental Figure 5G). Relative necrotic core in the lesions was slightly decreased by *Capn6* deficiency (Supplemental Figure 5H).

We investigated CAPN6 systemic expression in HFD-fed *Capn6*$^{-/y}$*Ldlr*$^{-/-}$ mice using a LacZ reporter assay (Figure 7D), as the mice express LacZ under the *Capn6* native promoter (20). As a result, transcriptional activity of *Capn6* is restricted in atherosclerotic plaques, but not in other organs. Immunohistochemistry showed CAPN6 expression in macrophages in atherosclerotic lesions (Figure 7E), but not in other vascular component cells, including endothelial cells and smooth muscle cells (Supplemental Figure 5I). Next, we evaluated CAPN6 expression in human atheromas (Figure 8; clinicopathologic information is available in Supplemental Table 1 and Supplemental Table 2). CAPN6 expression was negligible in adventitial macrophages in the normal aorta (Figure 8A). Conversely, CAPN6 was abundant in macrophages in severe coronary lesions. CAPN6 expression in human aortic atheromas was positively correlated with the severity of the lesions (Figure 8, B–D).

We assessed the contribution of myeloid *Capn6* to atherogenesis through BM transplantation experiments (Figure 9). PCR-based genotyping validated BM chimerism in recipient mice (*Capn6*$^{+/y}$ *Ldlr*$^{-/-}$ and *Capn6*$^{-/y}$*Ldlr*$^{-/-}$) transplanted with BM cells of different genotypes (Figure 9A). Transplantation of *Capn6*$^{-/y}$*Ldlr*$^{-/-}$ BM cells significantly decreased HFD-induced aortic atherosclerotic lesions compared with transplantation of *Capn6*$^{+/y}$*Ldlr*$^{-/-}$ BM cells independently of the recipient genotype (Figure 9B).

Using methods reported by Tacke et al. (21), we conducted in vivo labeling of circulating Ly-6C^{hi} monocytes to evaluate the recruitment of proatherogenic macrophages into the atherosclerotic lesions (Figure 10A). Subsequent to the transient depletion of preexisting monocytes by clodronate liposome, recruitment

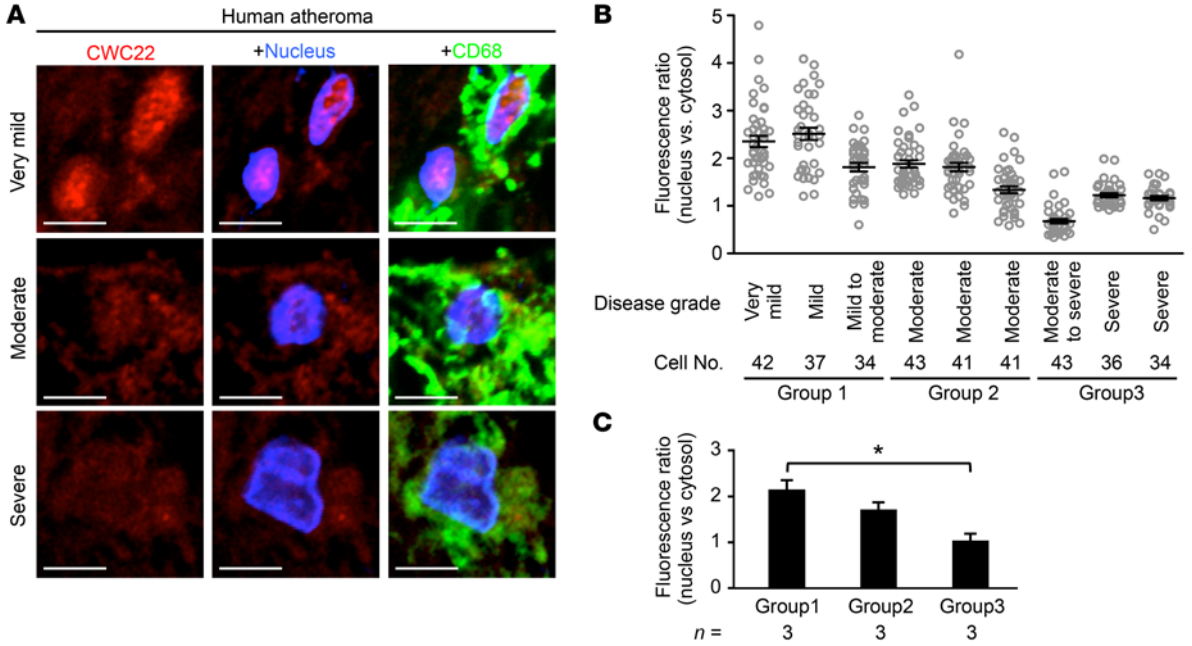

Figure 5. Nuclear localization of CWC22 in human macrophages/foam cells is negatively correlated with atherosclerosis grade. (**A**) Representative micrographs of CWC22 subcellular distributions in macrophages/foam cells in human atherosclerotic lesions in aorta. Scale bars: 5 μm.(**B**) Nuclear localization of CWC22 in CD68-positive cells was quantified with respect to each specimen. (**C**) Statistical comparison of CWC22 nuclear localization in human macrophages/foam cells. Specimens were divided into 3 groups based on the atherosclerosis grade. *$P < 0.05$, 1-way ANOVA followed by Bonferroni's test (**C**); error bars represent mean ± SEM.

of latex-positive monocytes into the aortic lesions was evaluated at day 3 following i.v. injection of latex beads. Whereas uptake of latex in circulating monocytes was equivalent between *Capn6*$^{+/y}$ *Ldlr*$^{-/-}$ and *Capn6*$^{-/y}$*Ldlr*$^{-/-}$ mice (Figure 10A), the number of latex-positive cells in atherosclerotic lesions was reduced by *Capn6* deficiency (Figure 10B). Importantly, preexisting foam cell macrophages, but not newly recruited monocytes, abundantly express CAPN6 (Figure 10C and Supplemental Figure 6A), indicating that CAPN6 in monocytes/macrophages is induced after the cells infiltrate into lesions. Consistently, expression of the macrophage marker CD68 and macrophage accumulation in atherosclerotic lesions in the mice fed HFD for 12 weeks were reduced by *Capn6* deficiency (Figure 10, D and E), whereas the expression of the inflammatory molecules *Icam1*, *Vcam1*, *Sele*, *Tnfa*, *Il1b*, *Il6*, and *Ccl2* (Supplemental Figure 6B), as well as of the lymphocyte markers *Cd4* and *Cd8a1* (Figure 10D), remained unchanged. Filipin III–based cholesterol staining in macrophages in murine atheromas showed that *Capn6* deficiency reduced the amount of cholesterol in individual macrophages (Figure 10F), whereas it did not affect expression of genes related to the receptor-mediated uptake of oxidized LDL and its subsequent processing, including *Msr1*, *Cd36*, *Abca1*, *Abcg1,* and *Acat1* (Supplemental Figure 6C).

We assessed the in vivo uptake of fluorescent nanoparticles in macrophages as an index of pinocytotic activity (Figure 10G). Pinocytotic activity in macrophages in *Capn6*$^{-/y}$*Ldlr*$^{-/-}$ atheromas was significantly lower than that in *Capn6*$^{+/y}$*Ldlr*$^{-/-}$ lesions. Immunohistochemical analysis showed that nuclear localization of CWC22 was relatively frequent in macrophage foam cells in *Capn6*$^{-/y}$*Ldlr*$^{-/-}$ atheromas than in *Capn6*$^{+/y}$*Ldlr*$^{-/-}$ atheromas (Figure 11A). *Capn6* deficiency upregulated the splicing efficiency of *Rac1* and *Tpi1* mRNA but not of *Rhoa* mRNA in the proatherogenic aortas of *Ldlr*$^{-/-}$ mice (Figure 11B), a phenomenon accompanied by the elevated Rac1 protein expression in the whole aorta, while RhoA protein expression remained unchanged (Figure 11C). BM transplantation experiments showed that *Rac1* splicing upregulation was dependent on *Capn6* expression in myeloid cells (Supplemental Figure 6D). Immunohistochemical analysis demonstrated that *Capn6* deficiency upregulated Rac1 protein expression in macrophages in atherosclerotic plaques (Figure 11D).

Discussion

Although it is established that macrophages uptake LDL and adopt foam cell properties, the specific mechanisms underlying the hyperpinocytosis of native LDL by macrophages evident under inflammatory conditions remain elusive. Our results show that pinocytotic activity, as well as cellular and intracellular dynamics in inflamed macrophages, depended on induction of CAPN6 (Figure 1, E and G, and Figure 3C). *Capn6* deficiency counteracted progression of atherosclerosis as well as macrophage pinocytotic ability and deposition in the lesions (Figure 7B and Figure 10, E and G); thus, CAPN6 conferred atherogenicity to the inflamed macrophages. Unexpectedly, CAPN6 failed to induce global changes in mRNA expression; however, *Capn6* deficiency elevated efficiency of mRNA splicing in certain genes. Consequently, for what we believe is the first time, we have shown that the CWC22/EJC posttranscriptional splicing system is disturbed by a physical interaction with CAPN6, which confers the ability to pinocytose LDL under inflammatory conditions to macrophages, resulting in cholesterol deposition in the atheroprone vascular wall (Figure 11E).

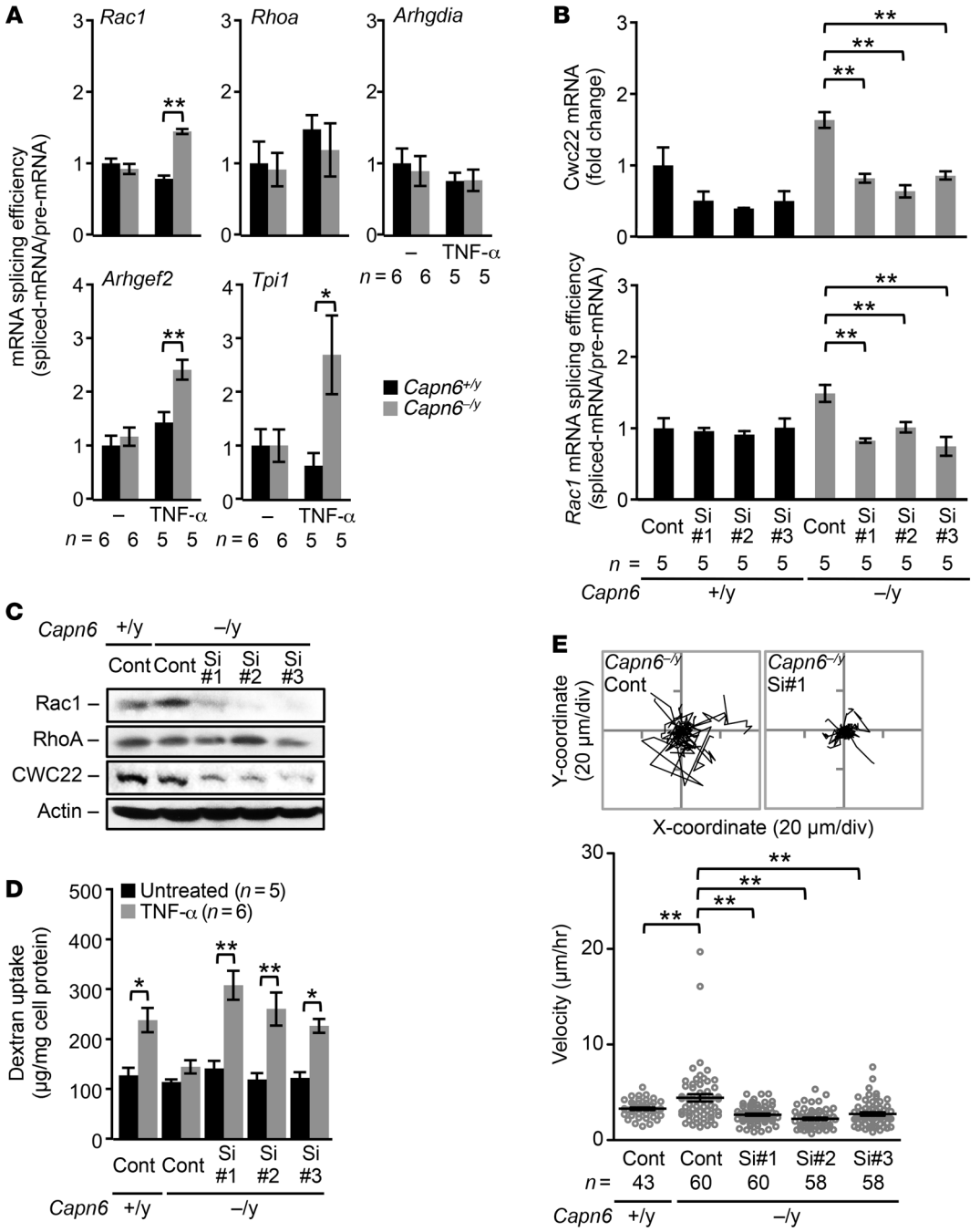

Figure 6. Rac1 downregulation in hyperpinocytotic macrophages is due to a disorder of CWC22-mediated mRNA splicing by CAPN6. BMMs differentiated with M-CSF/TNF-α for 4 days were used in these experiments. (**A**) Splicing of *Rac1, Arhgef2,* and *Tpi1* pre-mRNA but not of *Rhoa* and *Arhgdia* pre-mRNA is upregulated by *Capn6* deficiency. Spliced mRNA, pre-mRNA ratio served as a statistical value. (**B**) siRNA-based silencing of *Cwc22* abrogates the upregulated *Rac1* splicing caused by *Capn6* deficiency. (**C**) Silencing of *Cwc22* cancels the upregulation of Rac1 protein expression caused by *Capn6* deficiency. One representative result of 3 independent experiments is shown. Con, control; Si, siRNA. (**D**) Impaired pinocytotic activity in $Capn6^{-/y}Ldlr^{-/-}$ BMMs is rescued by silencing of *Cwc22*. (**E**) Accelerated cellular motility in $Capn6^{-/y}Ldlr^{-/-}$ BMMs is diminished by silencing of *Cwc22*. BMMs were stimulated with CCL2 at 50 ng/ml. $^{**}P < 0.01$; $^{*}P < 0.05$, 1-way ANOVA followed by Bonferroni's test (**A**, **B**, **D** and **E**); error bars represent mean ± SEM.

CAPN6 is primarily expressed in the foam cell macrophages in the human and murine atherosclerotic lesions (Figure 7E and Figure 8). Actually, current BM transplantation experiments showed that *Capn6* in BM-derived cells, but not in other vascular component cells in the lesions, is responsible for atherogenesis (Figure 9B), suggesting the dominant contribution of macrophage CAPN6 to atherogenesis. Reportedly, small GTPase signals orchestrate pinocytotic activity in certain cell types, including macrophages. Particularly, Rac1 GTPase mediates pinocytotic membrane transport (22) and membrane ruffling (23). Pharmacologic inhibition of Rho family GTPases by *C. difficile* toxin B diminishes the pinocytotic uptake of native LDL, even in macrophages (9, 18), whereas that of RhoA

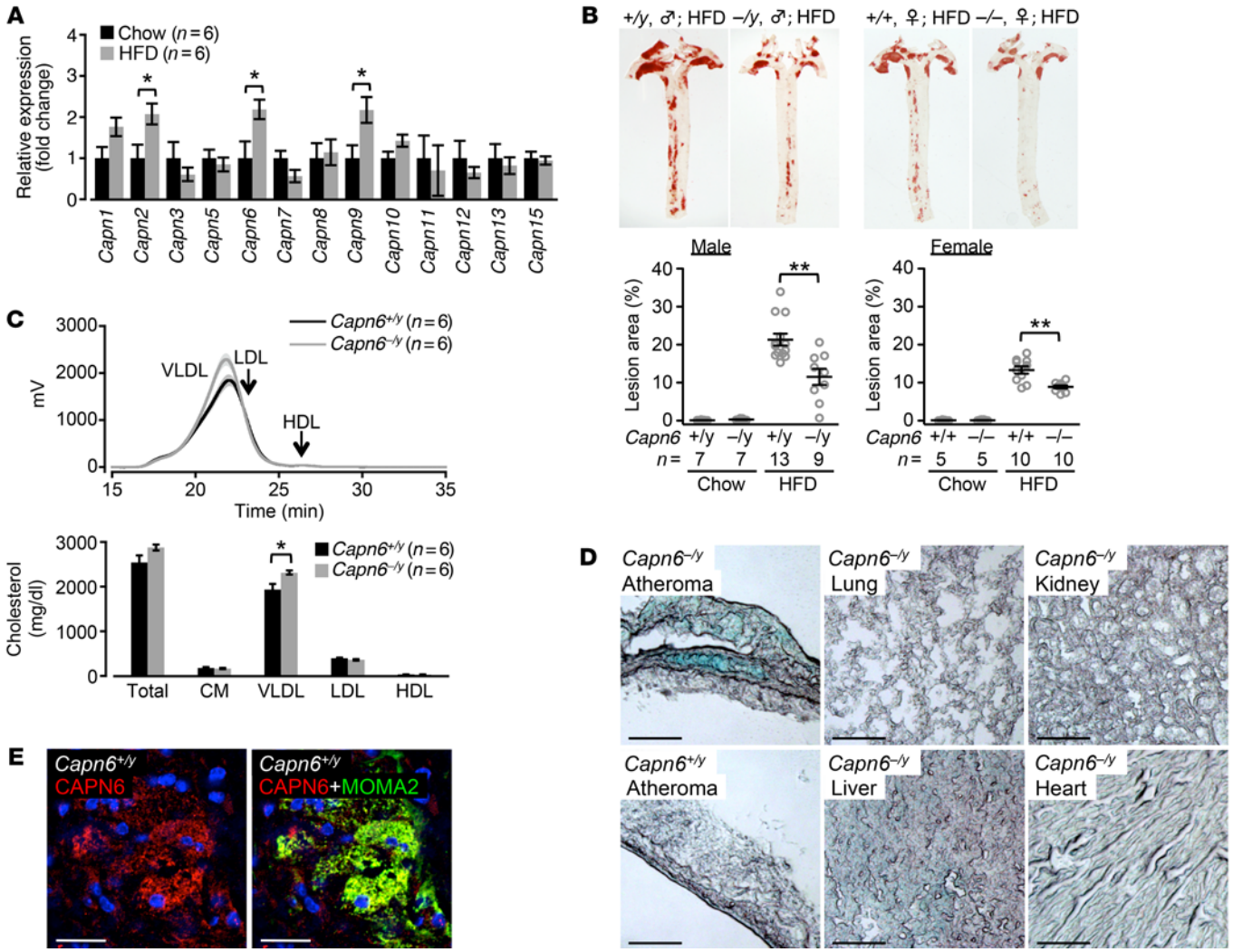

Figure 7. CAPN6 is induced in murine atheromas and exacerbates atherosclerotic diseases. (**A**) Aortic expression of calpain family genes in chow- or HFD-fed *Ldlr*$^{-/-}$ mice. Mice received chow or HFD for 12 weeks. (**B**) Loss of *Capn6* reduces aortic atherosclerosis in *Ldlr*$^{-/-}$ mice independently of sex. (**C**) *Capn6* deficiency does not ameliorate plasma dyslipidemia in *Ldlr*$^{-/-}$ mice. (**D**) *Capn6* promoter is activated specifically in atherosclerotic lesions. *Capn6*$^{+/y}$*Ldlr*$^{-/-}$ mice served as a negative control. (**E**) CAPN6 was localized in macrophages in murine atherosclerotic lesions. MOMA2 served as a macrophage marker. $^{**}P < 0.01$; $^{*}P < 0.05$, 1-way ANOVA followed by Bonferroni's test (**A**, **B** and **C**); error bars represent mean ± SEM. Scale bars: 100 μm (**D**); 25 μm (**E**).

or Rac1 fails to abolish pinocytotic uptake in these cells (18); thus, the contribution of individual Rho GTPases to pinocytotic activity in macrophages remains unclear. Our data indicate that *Capn6* deficiency restores the reduced expression of the Rac1 and GEF2 proteins evident in M-CSF/TNF-α–primed BMMs without altering the expression of the RhoA and RhoGDIα proteins, leading to the recovery of Rac1 activity in cells (Figure 2, A and B). This is consistent with an earlier investigation indicating that siRNA-based silencing of *CAPN6* in NIH3T3 cells potentiates Rac1 activity (24). This Rac1 system recovery appears to abrogate pinocytotic ability in *Capn6*$^{-/y}$ *Ldlr*$^{-/-}$ BMMs (Figure 2, C and E), while it slightly accelerates the production of oxidative stress and efferocytic activity in the cells (Supplemental Figure 2, G and H, respectively). It is noteworthy that the latter 2 phenotypes are likely to be pathophysiologically insignificant, since the changes in oxidative stress and the necrotic core by *Capn6* deficiency in the murine atherosclerotic lesion was marginal (Supplemental Figure 5, F and H, respectively). Importantly, Fujii et al. noted that prolonged Rac1 activity impairs the integration of RAB21 into pinosomes in macrophages (10), suggesting that Rac1 signaling delays pinosome maturation. This is consistent with our finding that the recovery of Rac1 activity by *Capn6* deficiency suppressed the integration of RAB5 into pinosomes and their lysosomal transition without altering pinosome density (Figure 3A and Supplemental Figure 3). While *Capn6* deficiency abrogates the pinosomal maturation in BMMs, pinocytotic particles in *Capn6*$^{-/y}$*Ldlr*$^{-/-}$ BMMs were preferentially transferred into RAB11-positive recycling vesicles (Figure 3A), which probably led to subsequent leakage of the particles to the extracellular space (Figure 3B). Our data further showed that the overexpression of wild-type Rac1 failed to decrease pinocytotic activity in BMMs (Supplemental Figure 2B), suggesting that Rac1 induction is necessary but insufficient for downregulation of pinocytotic activity in the cells. It is thought that the unknown mechanism or mechanisms that switch Rac1 into antipinocytosis action are activated by *Capn6* deficiency together with the Rac1

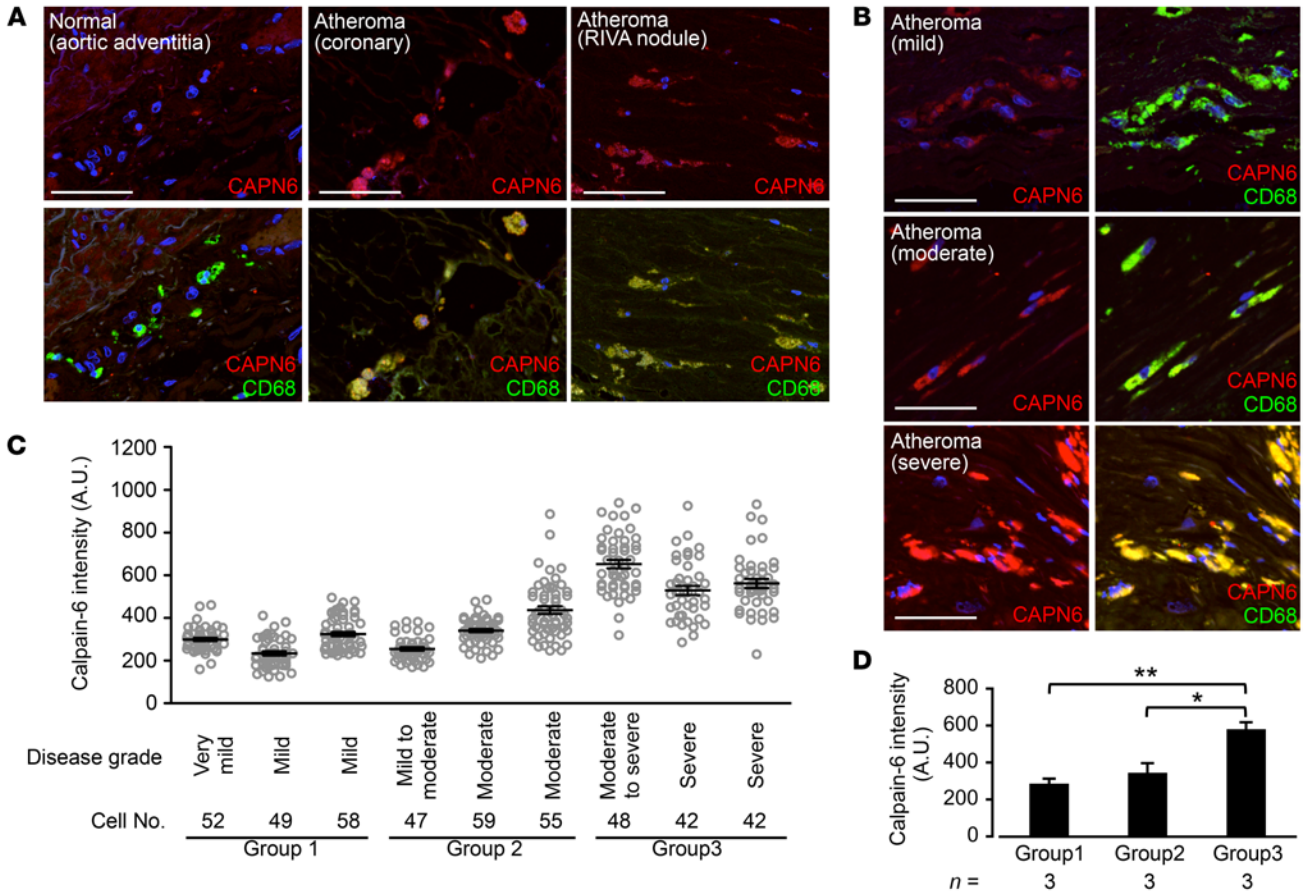

Figure 8. CAPN6 is localized in macrophages/foam cells in human moderate-to-severe atheromas. (**A**) CAPN6 expression in macrophages in human normal aorta and severe coronary atheromas. (**B**) CAPN6 expression in macrophages in human aortic atheromas. Scale bars: 50 μm (**A** and **B**). (**C**) CAPN6 expression in CD68-positive cells was quantified with respect to each specimen. (**D**) Statistical comparison of CAPN6 expression in human macrophages/foam cells. Specimens were divided into 3 groups based on the atherosclerosis grade. CD68 served as a macrophage marker. Arrows represent CAPN6-positive macrophages. $^{**}P < 0.01$; $^{*}P < 0.05$, 1-way ANOVA followed by Bonferroni's test (**D**).

inductions. In contrast, our pharmacologic data did not prove the contribution of RhoA signaling to pinocytotic activity in *Capn6*$^{-/y}$ *Ldlr*$^{-/-}$ BMMs (Figure 2C). Collectively, *Capn6* abrogates Rac1 signaling and accelerates pinosomal maturation in macrophages rather than participating in the pinosome formation. This may confer hyperpinocytosis on inflamed macrophages.

Although our present data showed that *Capn6* deficiency facilitated the movement of BMMs in response to CCL2 (Figure 1E), it inconsistently limited the recruitment and deposition of macrophages in murine atherosclerotic lesions (Figure 10, B, D, and E). It is noteworthy that the newly recruited monocytes in the atherosclerotic lesions did not express CAPN6, while preexisting foam cell macrophages were enriched with CAPN6 (Figure 10C and Supplemental Figure 6A), indicating that CAPN6 in monocytes/macrophages was induced after infiltration into the lesions. Thus, the recruitment of circulating monocytes may be independent of their endogenous CAPN6, while the exact mechanisms by which CAPN6 facilitated the recruitment are currently unclear. The abundance of CAPN6 in the preexisting macrophages, in turn, can limit their motility, thereby decelerating the emigration of the cells from the lesions. Therefore, it is possible for upregulation of CAPN6 to reduce the clearance of macrophages in atherosclerotic lesions.

Our in vitro DNA array and quantitative PCR (qPCR) analysis showed that the majority of the mRNA expression was comparable between *Capn6*$^{+/y}$*Ldlr*$^{-/-}$ and *Capn6*$^{-/y}$*Ldlr*$^{-/-}$ BMMs (Supplemental Figure 1, D and E). Similarly, the expression of *Icam1*, *Vcam1*, *Sele*, *Tnfa*, *Il1b*, *Il6*, *Ccl2*, *Msr1*, *Cd36*, *Abca1*, *Abcg1*, and *Acat1* in whole aorta was unchanged by *Capn6* deficiency, even with reducing macrophage number in the vessels (Supplemental Figure 6, B and C). Distinct changes in macrophage number and gene expression in the vessels indicated that the *Capn6*-driven proatherogenic macrophages have a negligible impact on the net gene expression in the vessels. A lack of global changes in gene expression in *Capn6*-deficient macrophages eliminated the possibility that their phenotypes were due to transcriptional regulation. Recent advances in macrophage biology revealed that the posttranscriptional processing of pre-mRNAs, in addition to their transcriptional regulation, modifies the fate of macrophages under inflammatory conditions (25). This pre-mRNA processing is driven by the spliceosome, a large ribonucleoprotein complex, and is mediated through RNA-binding proteins that form messenger ribonucleoprotein complexes (mRNPs) (26). A key regulatory element within mRNPs is EJC. EJC, which comprises 4 subunits — eIF4A3 (DDX48), MAGOH, Y14 (RBM8A), and BTZ (CASC3, MLN51; ref.

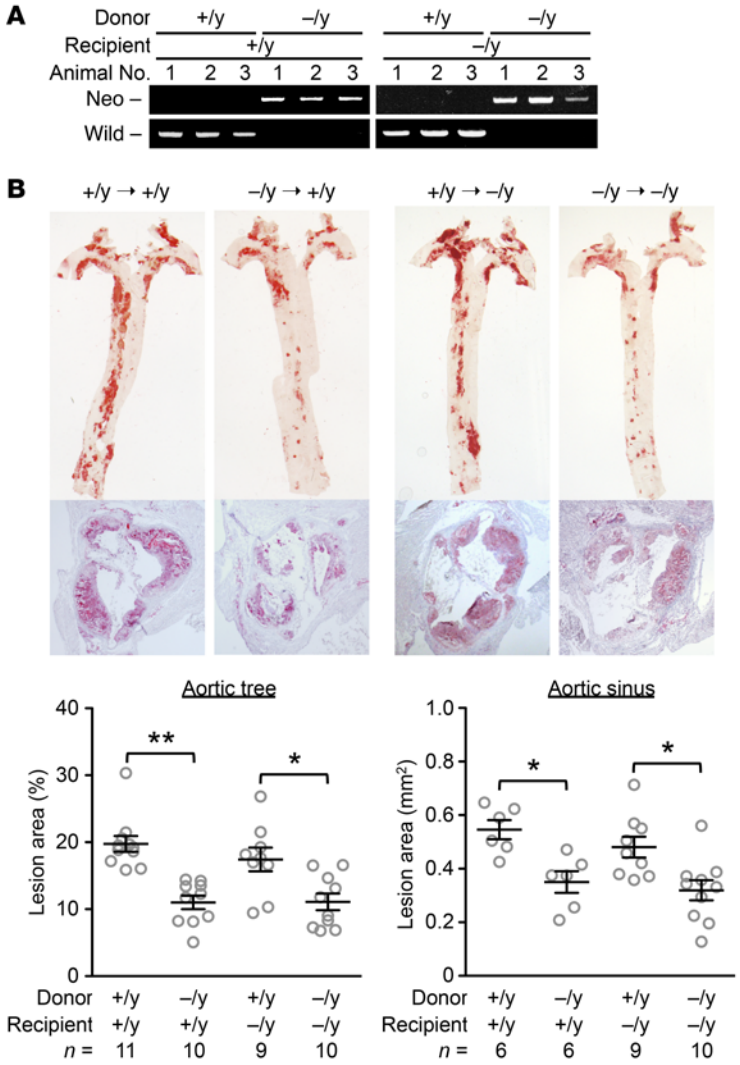

Figure 9. Myeloid *Capn6* is rate limiting for atherogenesis. (**A**) BM cells (1×10^7 cells/mouse) isolated from *Capn6*$^{+/y}$*Ldlr*$^{-/-}$ or *Capn6*$^{-/y}$*Ldlr*$^{-/-}$ donor mice were i.v. injected into x-ray–irradiated (8 Gy) *Capn6*$^{+/y}$*Ldlr*$^{-/-}$ or *Capn6*$^{-/y}$*Ldlr*$^{-/-}$ recipient mice. The *Capn6* genotype in BM cells from chimeric and nonchimeric mice was determined by a PCR-based analysis. (**B**) *Capn6* deficiency in BM cells, but not in resident cells, reduces atherosclerotic lesions. $^{**}P < 0.01$; $^{*}P < 0.05$, 1-way ANOVA followed by Bonferroni's test (**B**); error bars represent mean ± SEM.

27) — is known to bind to CWC22, an essential EJC-loading factor (19). Although binding of CWC22 to the EJC is indispensable for EJC-mediated splicing, their roles in macrophage biology remain unclear. Through a comprehensive protein-protein interaction analysis, we identified that CAPN6 is a CWC22-associated protein (Table 1) and that CWC22 nuclear localization is limited by the physical cytoplasmic interaction between CAPN6 and CWC22 (Figure 4, B, D, and E). Furthermore, we revealed that CWC22 was enriched in the nucleus in response to many inflammatory stimuli (Figure 4C). Interestingly, Singh et al. noted that MAGOH, a core component of the EJC, is induced in lipopolysaccharide-stimulated macrophages (28), suggesting that inflammatory signaling modifies CWC22/EJC-mediated mRNA processing. Current cell-based experiments suggest that *Cwc22* silencing reverses the macrophage phenotypes induced by *Capn6* deficiency, such as the recovery of Rac1 signaling, reduction in pinocytotic activity, and promotion of cellular movements (Figure 6, C–E); thus, the CWC22/EJC system dominates the phenotypic changes in *Capn6*-deficient BMMs. Importantly, the nuclear localization of CWC22 was negatively correlated with atherosclerosis grade in human patients (Figure 5) and was almost imperceptible in macrophages in severe atherosclerotic lesions in which CAPN6 is abundant (Figure 8). Thus, it is likely that CAPN6 limits the activity of the CWC22/EJC system in foam cells during atherogenesis, even in humans.

CAPN6 was first cloned by Dear et al. (29). CAPN6 expression is reportedly detectable in fetal skeletal muscle and in the placenta (20); however, its expression in skeletal muscle vanishes during growth. A gene-targeting study showed that CAPN6 limits the development and regeneration of skeletal muscle (20), although the physiologic and pathophysiologic role of this molecule remains unclear. Hong et al. noted that CAPN6 is induced during the differentiation of osteoclasts from BM-derived cells by receptor activator of NF-κB ligand, thereby accelerating bone-resorptive activity (30), suggesting that CAPN6 may function in the monocyte/macrophage lineage under certain conditions. Our data also revealed that CAPN6 is induced by proatherogenic mediators (Figure 1B) and switches macrophages to a hyperpinocytotic and immotile phenotype through disturbance of the CWC22/EJC system (Figure 6, D and E). CAPN6 is robustly induced by TNF-α, whereas CWC22 is activated uniformly by multiple cytokine classes (Figure 4C); thus, it is likely that disturbance of the CWC22/EJC system occurs primarily in the presence of TNF-α. Considering the predominance of TNF-α in atherosclerotic diseases (31), it appears that CAPN6 acts as a molecular switch, conferring hyperpinocytosis on inflamed macrophages in atherosclerotic lesions.

We identified regulatory mechanisms underlying LDL metabolism in macrophages. This concept of CAPN6-induced disturbance of the CWC22/EJC system explains the mechanism activating pinocytotic abilities in macrophages in atherosclerotic lesions. Targeting CAPN6 to achieve normalization of the CWC22/EJC system may represent an efficient approach to suppressing proatherogenic pinocytosis because CAPN6 is specifically expressed in inflamed macrophages and CAPN6-induced disturbance of the CWC22/EJC system may be translatable into humans with atherosclerosis. To confirm the pathophysiologic significance of the CWC22/EJC system, future studies exploring the target genes of the CWC22/EJC system in response to inflammatory insults are necessary.

Methods

Reagents. All chemicals used were commercial products of the highest grade of purity available. The sources of these reagents are detailed in Supplemental Methods.

Mice. Mice were fed chow (CRF-1; Oriental Yeast Co.) or HFD (F2HFD1; CRF-1 supplemented with 16.5% fat, 1.25% cholesterol, and 0.5% sodium cholate; Oriental Yeast Co.) for 12 weeks from 8 weeks of

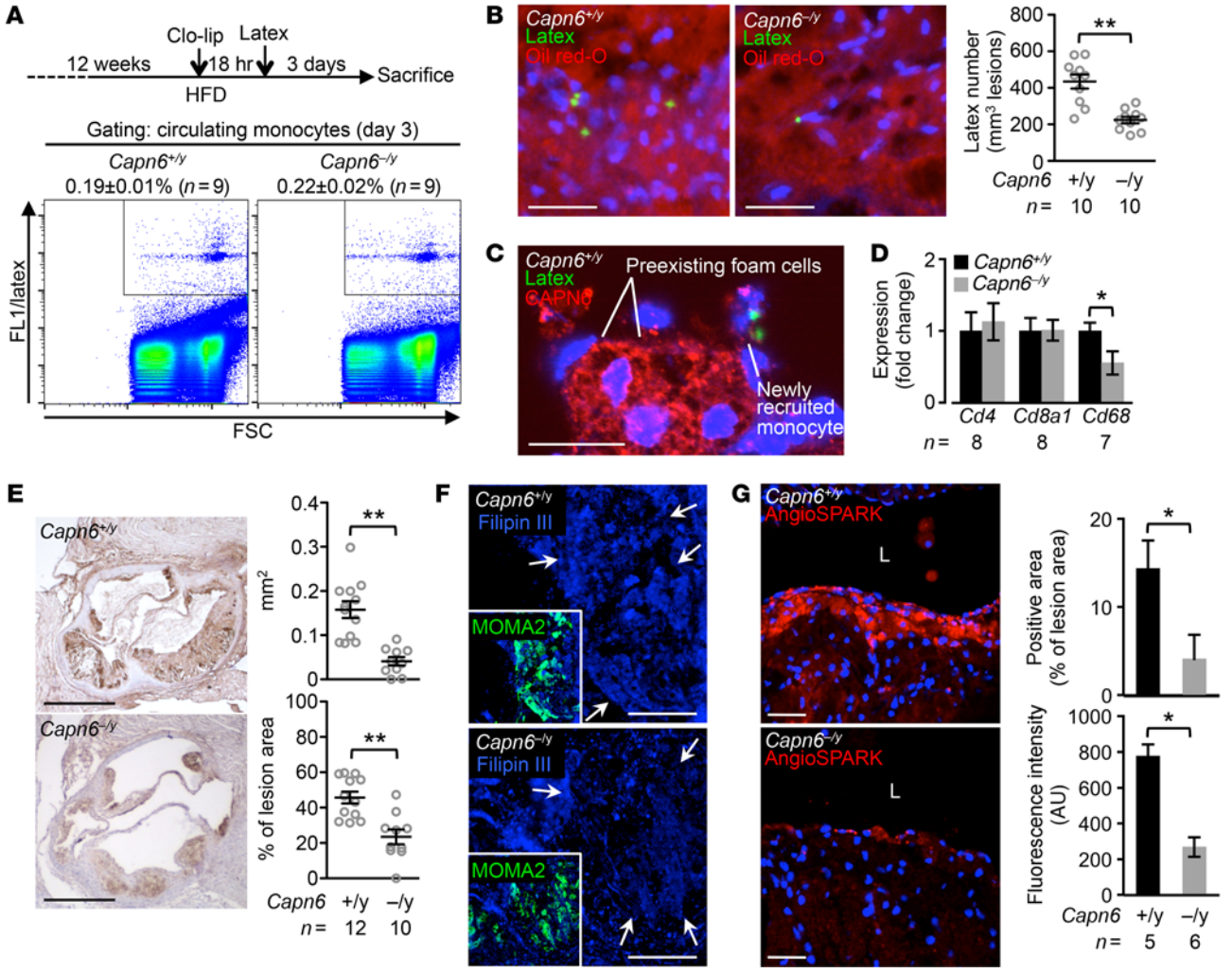

Figure 10. Ablation of CAPN6 diminishes the recruitment of macrophages and their pinocytotic ability in murine atherosclerotic lesions. (**A**) Uptake of latex beads in circulating monocytes at day 3 was equivalent between *Capn6*$^{+/y}$*Ldlr*$^{-/-}$ and *Capn6*$^{-/y}$*Ldlr*$^{-/-}$ mice. (**B**) Latex-positive monocytes in aortic atherosclerotic lesions were reduced by Capn6 deficiency. (**C**) CAPN6 expression is abundant in preexisting foam cell macrophages, but not in newly recruited macrophages, in *Capn6*$^{+/y}$*Ldlr*$^{-/-}$ atheromas. (**D**) PCR-based quantification of leukocyte markers in aortic atherosclerotic lesions in mice receiving HFD for 12 weeks. (**E**) Deposition of macrophages in atherosclerotic lesions is reduced by Capn6 deficiency. MOMA2^{+} area in aortic sinus lesions in the mice receiving HFD for 12 weeks was quantified. (**F**) Cholesterol deposition in atherosclerotic plaques. Aortic sections were stained with Filipin III. Arrows indicate macrophage-enriched regions. (**G**) Pinocytotic activity in atherosclerotic lesions. AngioSPARK nanoparticles were i.v. injected as a pinocytotic activity marker. L, aortic lumen. $^{**}P < 0.01$; $^{*}P < 0.05$; Student's *t* test (**D**, **E**, and **G**) and Mann-Whitney *U* test (**B**); error bars represent mean ± SEM. Scale bars: 50 μm (**B**); 20 μm (**C**); 500 μm (**E**); 100 μm (**F**); 40 μm (**G**).

age. Generation of *Capn6*- and *Capn9*-deficient mice was performed as described previously (20, 32). *Capn6*$^{-/y}$ mice express LacZ instead of CAPN6. *Ldlr*$^{-/-}$ mice (C57/BL6J) were obtained from The Jackson Laboratory (stock no. 2207). *Capn6*$^{-/y}$*Ldlr*$^{-/-}$ and *Capn9*$^{-/-}$*Ldlr*$^{-/-}$ mice were generated by intercrossing *Capn6*$^{-/y}$ and *Capn9*$^{-/-}$ mice with *Ldlr*$^{-/-}$ mice, respectively. *Capn6*$^{+/y}$*Ldlr*$^{-/-}$, *Capn6*$^{-/y}$*Ldlr*$^{-/-}$, *Capn9*$^{+/+}$*Ldlr*$^{-/-}$, and *Capn9*$^{-/-}$*Ldlr*$^{-/-}$ mice were maintained by homozygous breeding, as they have a common genetic background; the genotypes were determined by standard PCR-based genotyping with specific primers (Supplemental Table 3). High-sensitivity lipoprotein profiling was performed on EDTA plasma with the LipoSEARCH system equipped with a specific cholesterol detector by Skylight Biotech Inc.

BMMs. The isolation of BMMs was performed as described in our previous study (33). Briefly, murine BM cells were collected by flushing femoral BM with culture medium; subsequently, the cells were incubated in DMEM (Sigma-Aldrich) supplemented with 10% serum, penicillin–streptomycin–amphotericin B (Wako Pure Chemical Industries Ltd.), and M-CSF (50 ng/ml) for differentiation into macrophages in the presence or absence of the inflammatory cytokines TNF-α, IL-1β, IFN-γ, or IL-4 (10 ng/ml each). Unbound cells were removed by washing with medium; the culture medium was changed every other day.

Cellular movements. Measurement of cellular movements was described previously (34). Twenty thousand BMMs suspended in minimal essential medium were seeded on a 24-well culture plate. Then cellular movements in the presence of CCL2 (50 ng/ml) were monitored using a BioStation CT System (Nikon Instruments Inc.) at 37°C in a 5% CO_2 atmosphere under humidified conditions. Phase-contrast images were obtained at 60-minute intervals for 10 hours. Movement of cell centroids, calculated using ImageJ software (NIH), was measured to determine cell velocity as a statistical value.

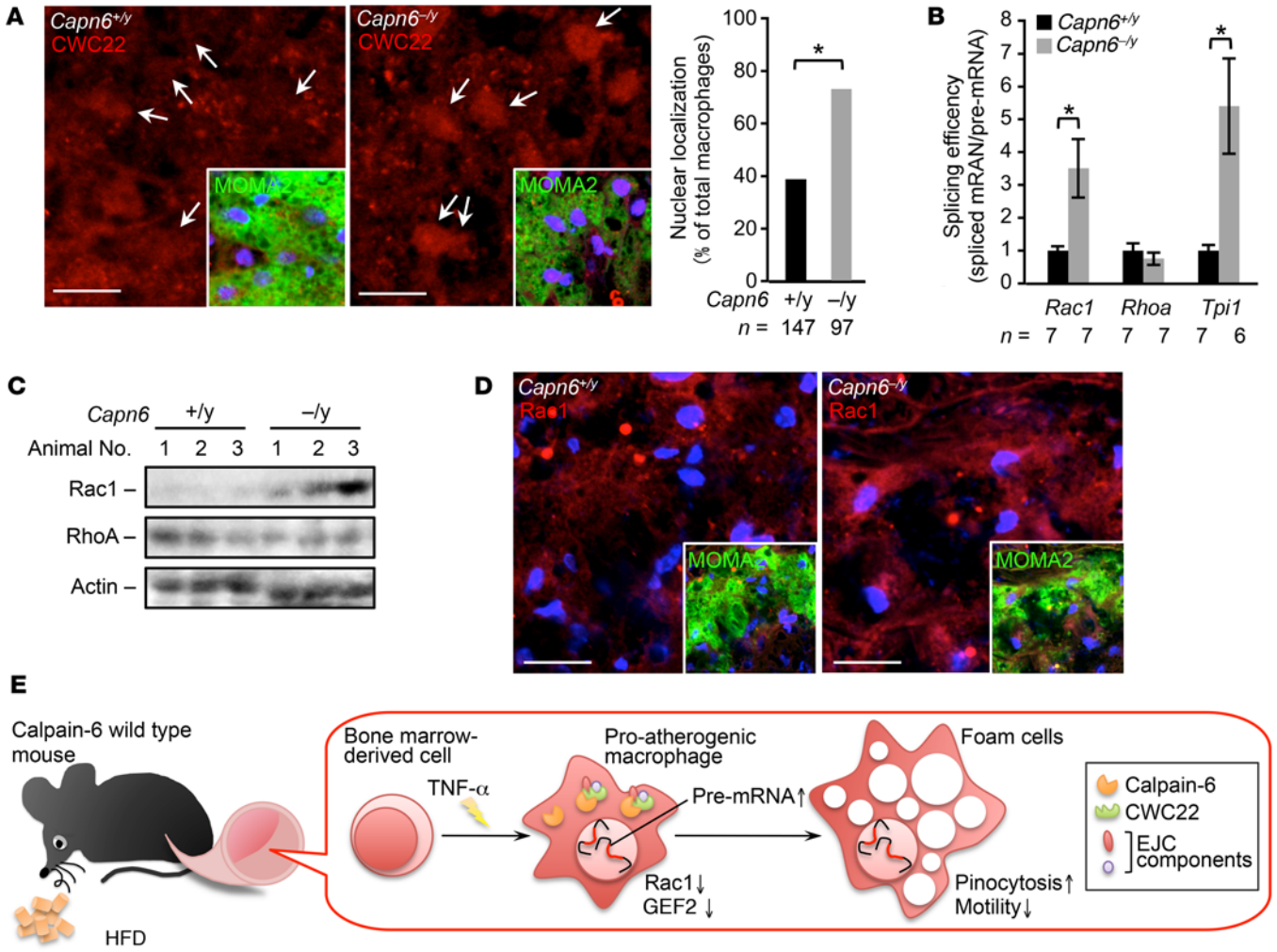

Figure 11. Loss of CAPN6 facilitates nuclear localization of CWC22 and subsequent *Rac1* splicing in macrophages/foam cells in murine atheromas. (**A**) Nuclear localization of CWC22 in macrophages in murine atheromas. MOMA2 served as a macrophage marker. Arrows represent nuclei. (**B**) Splicing of *Cwc22* mRNA is accelerated by loss of *Capn6*. Splicing efficiency in whole aorta was measured by a PCR-based analysis. (**C**) Protein expression of Rac1 but not of RhoA in proatherogenic aorta. Protein expression in whole aorta was evaluated by immunoblotting. (**D**) Immunohistochemical distribution of Rac1 protein in macrophages in atheromas. MOMA2 served as a marker for macrophages. (**E**) Schematic depiction of the CAPN6-mediated disturbance of posttranscriptional regulation in proatherogenic macrophages. CAPN6 was induced in *Capn6*$^{+/y}$ macrophages in response to TNF-α and was associated with CWC22 in the cytoplasm. This association disturbs the nuclear localization of CWC22, thereby suppressing posttranscriptional processing of *Rac1* and *Arhgef2* (the genes encoding Rac1 and GEF2, respectively) and potentiates subsequent pinocytotic responses. Thus, CAPN6 induction in macrophages facilitates atherosclerotic development. *$P < 0.05$, Fisher's exact test (**A**) and 1-way ANOVA followed by Bonferroni's test (**B**); error bars represent mean ± SEM. Scale bars: 10 μm (**A**); 20 μm (**D**).

In vitro uptake of native LDL and the pinocytosis assay. Human LDL (d = 1.019–1.063 g/ml) was prepared as described previously (16). To prepare oxidized LDL, native LDL (0.1 mg/ml) was incubated for 20 hours at 37°C with 5 μmol/l $CuSO_4$, followed by the addition of 1 mmol/l ethylenediaminetetraacetic acid and cooling. To measure the uptake of LDL-derived cholesterol, TNF-α/M-CSF–primed BMMs (3×10^4 cells) were seeded on a 96-well culture plate. Next, native or oxidized LDL was added to the culture medium and incubated for 24 hours. After washing 3 times with HBSS, cellular lipids were extracted using hexane-isopropanol (v/v 3:2; 100 μl/well). Then the extracts were transferred to another 96-well plate and dried. Cholesterol in the residue was quantified using a Cholesterol-E Kit (Wako Pure Chemical Industries Ltd.) and normalized against the total protein, which was measured by the bicinchoninic acid (BCA) method (Pierce Biotechnology Inc.). To measure pinocytotic activity, BMMs or J774 macrophages were exposed to TRITC-labeled dextran (molecular weight, 70,000) at 5 mg/ml for 24 hours. To evaluate the temporal changes in Dil-LDL uptake, BMMs were subjected to the mixture of Dil-labeled LDL (Alfa Aesar) and unlabeled LDL (mixture ratio: w/w 1:20) at 400 μg/ml. After washing 3 times with PBS, fluorescent dextran or Dil-labeled LDL uptake in the cells was measured using a microplate reader (Mithras LB 940; Berthold Technologies GmbH & Co. KG) or by confocal microscopy (A1; Nikon Instruments Inc.), as appropriate.

Rac1 activity. Rac1 activity in BMMs was measured using a Rac1 G-LISA Activation Assay Kit (Cytoskeleton, Inc.) according to the manufacturer's instructions. TNF-α/M-CSF–primed BMMs (2×10^5 cells) were stimulated with CCL2 at 50 ng/ml or native LDL at 400 μg/ml for 20 minutes and lysed in lysis buffer. Subsequently, protein was quantified

using the BCA assay (Pierce Biotechnology, Inc.); protein aliquots (0.6 mg/ml) were loaded into the assay plate. Active Rac1 bound to plate walls was probed using an anti-Rac1 antibody and a horseradish peroxidase–labeled secondary antibody. After the chemiluminescent reaction, optical absorbance at 490 nm was measured as an index of Rac1 activity.

Pinosome dynamics and maturation. BMMs were seeded onto collagen I-coated cover slips; then 5 mg/ml TRITC-labeled dextran was added to the culture medium to label the pinosomes. After 30 minutes, cells were washed 3 times with HBSS, and pinosomes in individual cells were tracked for 30 minutes at 1-minute intervals using confocal microscopy (A1; Nikon Instruments Inc.). The velocity and density of pinosomes were determined using ImageJ (NIH).

Leakage of pinocytotic particles. BMMs were differentiated in the presence of 10 ng/ml TNF-α and 50 ng/ml M-CSF for 3 days and were seeded onto 48-well culture plate (2×10^5 cells/well). Subsequently, the cells were loaded with TRITC-labeled dextran at 5 mg/ml in the presence or absence of NSC23766 at 50 μmol/l. After 24 hours of incubation, cells were washed 3 times with RPMI medium and were incubated with RPMI medium supplemented with 10 ng/ml TNF-α and 50 ng/ml M-CSF in the presence or absence of NSC23766 at 50 μmol/l. Subsequent to the incubation for 24 hours, the culture medium was collected and cells were lysed by PBS containing 0.4% Triton X-100. Detached cells and unlysed debris in the culture medium and cell lysate were removed by centrifugation; then fluorescent dextran in the culture medium or cell lysates were measured using a microplate reader (Mithras LB 940; Berthold Technologies GmbH & Co. KG; Ex/Em: 530/590 nm). Dextran leakage was calculated from the following equation: dextran leakage = $[F_{media}/(F_{cell} + F_{media})] \times 100\%$, where F_{media} represents fluorescence intensity in the culture medium and F_{cell} denotes fluorescence intensity in cell lysate.

IP–LC–MS/MS. LC-MS/MS analysis was used as described previously (35). J774 cells were a gift from Masamichi Takami (Showa University School of Dentistry, Tokyo, Japan). J774 cells were transfected with vectors encoding GFP alone or GFP-fused *Capn6* using Lipofectamine 3000 (Invitrogen). Twenty-four hours after transfection, tagged proteins were collected by IP using anti-GFP antibody (Clontech Laboratories Inc.) and were eluted using citrate buffer (pH 2–3). The eluent was then blotted onto PVDF membranes, and the membranes were dried out. Subsequently, the membranes were incubated with a DTT-based reaction solution (80 mmol/l NH_4HCO_3, 10 mmol/l DTT, and 20% acetonitrile) at 56°C for 1 hour. The reaction solution was then replaced with iodoacetamide solution (80 mmol/l NH_4HCO_3, 55 mmol/l iodoacetamide, and 20% acetonitrile) and incubated at room temperature for 45 minutes in the dark. Following washing with distilled water and 2% acetonitrile, the membranes were incubated overnight with 1 μg of trypsin dissolved into 30 mmol/l NH_4HCO_3 containing 70% acetonitrile. The tryptic digests were extracted twice with 70% acetonitrile/1% TFA and were dried out using a SpeedVac evaporator (Thermo Fisher Scientific). The residues were dissolved in 0.2% formic acid and analyzed using a Triple TOF5600 System (AB SCIEX). Data were analyzed by ProteinPilot Software (AB SCIEX) to explore the candidate CAPN6-associated proteins. Proteins that were precipitated similarly in GFP-expressing J774 lysates (GFP tag alone) were omitted from the candidate proteins.

PCR-based detection of mRNA splicing. To evaluate the efficiency of mRNA splicing, expression levels of pre-mRNAs and spliced mRNAs were measured by qPCR. The analytic principles and primer designs are detailed in Supplemental Figure 4. The expression ratio of spliced mRNA to pre-mRNA served as an index of splicing efficiency. To avoid contamination with genomic DNA, total RNA was treated with DNase I (Invitrogen) before the reverse-transcription reaction.

BM transplantation. BM transplantation was conducted as previously described (33). To eliminate resident BM cells, recipient mice (*Capn6*$^{+/y}$*Ldlr*$^{-/-}$ or *Capn6*$^{-/y}$*Ldlr*$^{-/-}$) were x-ray–irradiated at 8 Gy for 10 minutes using a soft x-ray system (OM-150HTS; OHMiC). The next day, BM cells (1×10^7 cells/animal) isolated from donor mice (*Capn6*$^{+/y}$*Ldlr*$^{-/-}$ or *Capn6*$^{-/y}$*Ldlr*$^{-/-}$) were i.v. injected into recipient mice. Four weeks later, mice received HFD to induce atherosclerotic disease. Successful replacement of BM cells was validated by PCR-based genotyping of the BM.

In vivo tracking of circulating monocytes. In vivo labeling of circulating Ly-6C^{hi} monocytes was performed according to the previous literature by Tacke et al (21). Mice were fed HFD for 12 weeks, followed by i.v. injection of 200 μl of clodronate liposome (FormuMax Scientific Inc.) into tail vein to transiently deplete circulating monocytes. Eighteen hours later, 1.0-μm Fluoresbrite Plain YG Microspheres (w/v 2.5% solids; Polysciences Inc.) were diluted 1:25 in PBS, and 250 μl of the solution was injected into the mice via tail vein. After 3 days, mice were sacrificed, and aortic sinus and whole blood with EDTA were collected. Erythrocytes in the whole blood samples were lysed with BD Pharm Lyse (BD Biosciences); then the samples were analyzed by using BD FACSVerse (BD Biosciences) to evaluate the uptake of fluorescence beads in monocyte population. Aortic sinus was cryosectioned at a thickness of 10 μm and was stained with oil red O and DAPI. Latex beads in the atherosclerotic lesion sections were detected by using a conventional fluorescent microscope (IX70, Olympus) and were counted using ImageJ software (NIH).

In vivo pinocytosis activity. The detection of in vivo pinocytotic activity was performed as described previously (8). *Capn6*$^{+/y}$*Ldlr*$^{-/-}$ and *Capn6*$^{-/y}$*Ldlr*$^{-/-}$ mice that received a HFD for 12 weeks were used in these experiments. The mice were subjected to the i.v. administration of AngioSPARK 680 nanoparticles (PerkinElmer) at 80 mg/kg. After 24 hours, the mice were sacrificed; the aortic trees were dissected. The isolated aortas were cryosectioned; the uptake of fluorescent nanoparticles by the vascular wall was detected using confocal microscopy (A1; Nikon Instruments Inc.). Simultaneously, monocyte/macrophage antigen-2 (MOMA2) was immunohistochemically detected as a macrophage marker.

X-gal staining, immunohistochemistry, and quantification of atherosclerotic lesions. Because the targeted allele in *Capn6*-deficient mice contains the LacZ reporter, which is driven by the *Capn6* native promoter (20), we assessed the activity of *Capn6* using a β-Galactosidase Staining Kit (Takara Bio Inc.) according to the manufacturer's instructions. Briefly, isolated aortic tissues were immersed overnight in reaction buffer at 37°C. Subsequently, specimens were cryosectioned at 6-μm thickness and photographed using light microscopy. For immunohistochemical analysis in mice, the isolated aortic trees and roots were fixed in 4% paraformaldehyde (PFA) in PBS and were subsequently frozen, sectioned at 6-μm thickness, and mounted on glass slides as required. Target molecules were detected using immunofluorescence histochemistry or conventional immunohistochemistry with specific antibodies (Supplemental Table 4). To quantify atherosclerotic lesions, PFA-fixed aortic trees and roots were stained with oil red O in 60% isopropanol for 30 minutes. The specimens were washed with 60% isopropanol and photographed to calculate the staining-positive areas using ImageJ (NIH).

DNA array. BMMs from 4 different mice were pooled in each mouse line to minimize the individual differences and were lysed using TRIzol Reagent (Invitrogen). The DNA array was conducted using an Agilent Expression Array (Agilent Technologies) and a SurePrint G3 Mouse GE 8 × 60 K Microarray (Agilent Technologies) in the Dragon Genomics Center (Takara Bio Inc.). Data were deposited in the NCBI's Gene Expression Omnibus (GEO GSE83815).

Immunohistochemical analysis in humans. To evaluate the nuclear localization of CWC22 in macrophages, atherosclerotic lesions in human aortic segments, collected from 10 autopsied patients (men, 5; women, 5; age, 39–86 years; Supplemental Table 1), were graded based on the American Heart Association's criteria (36). Antigen retrieval was performed by heat-induced epitope retrieval using citrate buffer (Sigma-Aldrich) for 5 minutes at 121°C. The expression of CWC22 protein in the segments was detected by fluorescent immunohistochemistry with anti-CWC22 antibody (Sigma-Aldrich). Meanwhile, a commercially available cardiovascular tissue microarray (Provitro AG), as well as the specimens noted above, was employed for immunohistochemical detection of CAPN6 expression. Antigen retrieval was performed using proteinase K (DAKO) for 15 minutes at room temperature; CAPN6 protein expression was detected by fluorescent immunohistochemistry with anti-CAPN6 antibody (Abcam). Clinicopathological information regarding the tissue microarray is available in Supplemental Table 2.

Statistics. Our results are expressed as mean ± SEM; statistical analyses were performed using GraphPad Prism 5 (GraphPad Software Inc.). Two-tailed Student's *t* test was used to compare 2 groups with equal variances; alternatively, Mann–Whitney *U* test was applied for data with unequal variances. Multiple comparisons were conducted with 1- or 2-way nonrepeated measures ANOVA followed by post-hoc Bonferroni's test, as appropriate. *P* values of less than 0.05 were considered statistically significant.

Study approval. All experimental procedures involving animals were approved by the Institutional Animal Care and Use Committee of Showa University and were conducted in conformity with the Animal Care and Use Committee Guidelines of Showa University. Use of human aortic autopsy specimens was approved by the Ethics Committee of Kumamoto University School of Medicine and was conducted in conformity with the Ethics Committee guidelines of Kumamoto University School of Medicine.

Author contributions

TM, KT, SH, HS, HK, and AM conceived the project and designed the experiments. TM conducted most of the experiments and data analyses. XFL and JRKK supported the experiments and data interpretations. KT generated *Capn6*$^{-/-}$ mice. SH generated *Capn9*$^{-/-}$ mice. KO and MT collected human autopsy specimens. TA and HI conducted IP–LC–MS/MS analysis. The manuscript was written and revised by TM and edited by AM.

Acknowledgments

The authors greatly appreciate Hideo Kataoka and Hirotaka Kuwata (Showa University School of Dentistry) for instruction on FACS analysis and valuable comments. This study was partially supported by the Japan Society for the Promotion of Science (JSPS) KAKENHI grant 26461368 (to AM), JSPS KAKENHI grant 15K09418 (to TM), CSTI-SIP BRAIN-NARO ID:14533567 (to HS), and research grants from the Takeda Science Foundation, the Banyu Life Science Foundation International, the NOVARTIS Foundation, the Ono Medical Research Foundation, a Hiroshi Irisawa, Aya Irisawa Memorial Research Grant from the Japan Heart Foundation and the Japan Heart Foundation & Astellas Grant for Research on Atherosclerosis Update (all to TM).

Address correspondence to: Takuro Miyazaki, Department of Biochemistry, Showa University School of Medicine, 1-5-8 Hatanodai, Shinagawa-ku, Tokyo 142-8555, Japan. Phone: 81.3.3784.8116; E-mail: taku@pharm.showa-u.ac.jp.

1. Weber C, Noels H. Atherosclerosis: current pathogenesis and therapeutic options. *Nat Med*. 2011;17(11):1410–1422.
2. Waters DD. What the statin trials have taught us. *Am J Cardiol*. 2006;98(1):129–134.
3. Cannon CP, et al. Intensive versus moderate lipid lowering with statins after acute coronary syndromes. *N Engl J Med*. 2004;350(15):1495–1504.
4. Brown MS, Goldstein JL. Lipoprotein metabolism in the macrophage: implications for cholesterol deposition in atherosclerosis. *Annu Rev Biochem*. 1983;52:223–261.
5. Steinbrecher UP, Lougheed M. Scavenger receptor-independent stimulation of cholesterol esterification in macrophages by low density lipoprotein extracted from human aortic intima. *Arterioscler Thromb*. 1992;12(5):608–625.
6. Manning-Tobin JJ, et al. Loss of SR-A and CD36 activity reduces atherosclerotic lesion complexity without abrogating foam cell formation in hyperlipidemic mice. *Arterioscler Thromb Vasc Biol*. 2009;29(1):19–26.
7. Kruth HS. Receptor-independent fluid-phase pinocytosis mechanisms for induction of foam cell formation with native low-density lipoprotein particles. *Curr Opin Lipidol*. 2011;22(5):386–393.
8. Buono C, Anzinger JJ, Amar M, Kruth HS. Fluorescent pegylated nanoparticles demonstrate fluid-phase pinocytosis by macrophages in mouse atherosclerotic lesions. *J Clin Invest*. 2009;119(5):1373–1381.
9. Anzinger JJ, et al. Native low-density lipoprotein uptake by macrophage colony-stimulating factor-differentiated human macrophages is mediated by macropinocytosis and micropinocytosis. *Arterioscler Thromb Vasc Biol*. 2010;30(10):2022–2031.
10. Fujii M, Kawai K, Egami Y, Araki N. Dissecting the roles of Rac1 activation and deactivation in macropinocytosis using microscopic photo-manipulation. *Sci Rep*. 2013;3:2385.
11. Jeong SY, Martchenko M, Cohen SN. Calpain-dependent cytoskeletal rearrangement exploited for anthrax toxin endocytosis. *Proc Natl Acad Sci U S A*. 2013;110(42):E4007–E4015.
12. Tsai JC, et al. The role of calpain-myosin 9-Rab7b pathway in mediating the expression of Toll-like receptor 4 in platelets: a novel mechanism involved in α-granules trafficking. *PLoS One*. 2014;9(1):e85833.
13. Sorimachi H, Ono Y. Regulation and physiological roles of the calpain system in muscular disorders. *Cardiovasc Res*. 2012;96(1):11–22.
14. Wang N, et al. A PEST sequence in ABCA1 regulates degradation by calpain protease and stabilization of ABCA1 by apoA-I. *J Clin Invest*. 2003;111(1):99–107.
15. Hori N, Hayashi H, Sugiyama Y. Calpain-mediated cleavage negatively regulates the expression level of ABCG1. *Atherosclerosis*. 2011;215(2):383–391.
16. Miyazaki T, et al. m-Calpain induction in vascular endothelial cells on human and mouse atheromas and its roles in VE-cadherin disorganization and atherosclerosis. *Circulation*. 2011;124(23):2522–2532.
17. Subramanian V, Uchida HA, Ijaz T, Moorleghen JJ, Howatt DA, Balakrishnan A. Calpain inhibition attenuates angiotensin II-induced abdominal aortic aneurysms and atherosclerosis in low-density lipoprotein receptor-deficient mice. *J Cardiovasc Pharmacol*. 2012;59(1):66–76.
18. Barthwal MK, Anzinger JJ, Xu Q, Bohnacker T, Wymann MP, Kruth HS. Fluid-phase pinocytosis of native low density lipoprotein promotes murine M-CSF differentiated macrophage foam

cell formation. *PLoS One*. 2013;8(3):e58054.
19. Steckelberg AL, Boehm V, Gromadzka AM, Gehring NH. CWC22 connects pre-mRNA splicing and exon junction complex assembly. *Cell Rep*. 2012;2(3):454–461.
20. Tonami K, et al. Calpain-6 deficiency promotes skeletal muscle development and regeneration. *PLoS Genet*. 2013;9(8):e1003668.
21. Tacke F, et al. Monocyte subsets differentially employ CCR2, CCR5, and CX3CR1 to accumulate within atherosclerotic plaques. *J Clin Invest*. 2007;117(1):185–194.
22. Ridley AJ. Rho proteins: linking signaling with membrane trafficking. *Traffic*. 2001;2(5):303–310.
23. Ridley AJ, Paterson HF, Johnston CL, Diekmann D, Hall A. The small GTP-binding protein rac regulates growth factor-induced membrane ruffling. *Cell*. 1992;70(3):401–410.
24. Tonami K, et al. Calpain-6, a microtubule-stabilizing protein, regulates Rac1 activity and cell motility through interaction with GEF-H1. *J Cell Sci*. 2011;124(Pt 8):1214–1223.
25. Bhatt DM, et al. Transcript dynamics of proinflammatory genes revealed by sequence analysis of subcellular RNA fractions. *Cell*. 2012;150(2):279–290.
26. Rodríguez-Navarro S, Hurt E. Linking gene regulation to mRNA production and export. *Curr Opin Cell Biol*. 2011;23(3):302–309.
27. Tange TØ, Shibuya T, Jurica MS, Moore MJ. Biochemical analysis of the EJC reveals two new factors and a stable tetrameric protein core. *RNA*. 2005;11(12):1869–1883.
28. Singh KK, Wachsmuth L, Kulozik AE, Gehring NH. Two mammalian MAGOH genes contribute to exon junction complex composition and nonsense-mediated decay. *RNA Biol*. 2013;10(8):1291–1298.
29. Dear N, Matena K, Vingron M, Boehm T. A new subfamily of vertebrate calpains lacking a calmodulin-like domain: implications for calpain regulation and evolution. *Genomics*. 1997;45(1):175–184.
30. Hong JM, Teitelbaum SL, Kim TH, Ross FP, Kim SY, Kim HJ. Calpain-6, a target molecule of glucocorticoids, regulates osteoclastic bone resorption via cytoskeletal organization and microtubule acetylation. *J Bone Miner Res*. 2011;26(3):657–665.
31. Brånén L, Hovgaard L, Nitulescu M, Bengtsson E, Nilsson J, Jovinge S. Inhibition of tumor necrosis factor-alpha reduces atherosclerosis in apolipoprotein E knockout mice. *Arterioscler Thromb Vasc Biol*. 2004;24(11):2137–2142.
32. Hata S, et al. Calpain 8/nCL-2 and calpain 9/nCL-4 constitute an active protease complex, G-calpain, involved in gastric mucosal defense. *PLoS Genet*. 2010;6(7):e1001040.
33. Kigawa Y, et al. NADPH oxidase deficiency exacerbates angiotensin II-induced abdominal aortic aneurysms in mice. *Arterioscler Thromb Vasc Biol*. 2014;34(11):2413–2420.
34. Miyazaki T, et al. Calpastatin counteracts pathological angiogenesis by inhibiting suppressor of cytokine signaling 3 degradation in vascular endothelial cells. *Circ Res*. 2015;116(7):1170–1181.
35. Obama T, Kato R, Masuda Y, Takahashi K, Aiuchi T, Itabe H. Analysis of modified apolipoprotein B-100 structures formed in oxidized low-density lipoprotein using LC-MS/MS. *Proteomics*. 2007;7(13):2132–2141.
36. Stary HC, et al. A definition of advanced types of atherosclerotic lesions and a histological classification of atherosclerosis. A report from the Committee on Vascular Lesions of the Council on Arteriosclerosis, American Heart Association. *Circulation*. 1995;92(5):1355–1374.